JGP Journal of General Physiology

ARTICLE

Zn^{2+}-induced changes in $Ca_v2.3$ channel function: An electrophysiological and modeling study

Felix Neumaier, Serdar Alpdogan, Jürgen Hescheler, and Toni Schneider

Loosely bound Zn^{2+} ions are increasingly recognized as potential modulators of synaptic plasticity and neuronal excitability under normal and pathophysiological conditions. $Ca_v2.3$ voltage-gated Ca^{2+} channels are among the most sensitive targets of Zn^{2+} and are therefore likely to be involved in the neuromodulatory actions of endogenous Zn^{2+}. Although histidine residues on the external side of domain I have been implicated in the effects on $Ca_v2.3$ channel gating, the exact mechanisms involved in channel modulation remain incompletely understood. Here, we use a combination of electrophysiological recordings, modification of histidine residues, and computational modeling to analyze Zn^{2+}-induced changes in $Ca_v2.3$ channel function. Our most important findings are that multiple high- and low-affinity mechanisms contribute to the net Zn^{2+} action, that Zn^{2+} can either inhibit or stimulate Ca^{2+} influx through $Ca_v2.3$ channels depending on resting membrane potential, and that Zn^{2+} effects may persist for some time even after cessation of the Zn^{2+} signal. Computer simulations show that (1) most salient features of $Ca_v2.3$ channel gating in the absence of trace metals can be reproduced by an obligatory model in which activation of two voltage sensors is necessary to open the pore; and (2) most, but not all, of the effects of Zn^{2+} can be accounted for by assuming that Zn^{2+} binding to a first site is associated with an electrostatic modification and mechanical slowing of one of the voltage sensors, whereas Zn^{2+} binding to a second, lower-affinity site blocks the channel and modifies the opening and closing transitions. While still far from complete, our model provides a first quantitative framework for understanding Zn^{2+} effects on $Ca_v2.3$ channel function and a step toward the application of computational approaches for predicting the complex actions of Zn^{2+} on neuronal excitability.

Introduction

Voltage-gated Ca^{2+} channels (VGGCs) participate in neuronal signaling and provide the key link between electrical signals and various nonelectrical processes, such as neurotransmitter release, transcription, and muscle contraction (Catterall, 1998; Hofmann et al., 1999; Neumaier et al., 2015). Their modulation by foreign (i.e., non-Ca^{2+}) inorganic cations has proven instrumental in identifying the mechanisms underlying Ca^{2+}-selective flux and may have important (patho)physiological implications. For example, the d-block metal ions Zn^{2+} and Cu^{2+} have been identified as endogenous modulators of neuronal transmission and synaptic plasticity and implicated in a number of pathophysiological conditions (Frederickson et al., 2000, 2005; Mathie et al., 2006). $Ca_v2.3$ channels, which are thought to be involved in synaptic transmission (Gasparini et al., 2001), action potential burst firing, and oscillatory activity (Christie et al., 1995; Magee and Carruth, 1999), are among the most sensitive targets for Zn^{2+} and Cu^{2+} currently known (Kang et al., 2007; Shcheglovitov et al., 2012). In addition, these channels have an expression pattern that coincides with the spatial distribution of loosely bound Zn^{2+} ions in the brain (Sochivko et al., 2002; Weiergräber et al., 2006b), suggesting that they could represent a main mediator for the reported anticonvulsive effects of endogenous Zn^{2+}. Although nonconserved histidine residues in the voltage-sensor module (VSM) of domain I have been convincingly implicated in the effects of Zn^{2+} on $Ca_v2.3$ channel gating (Fig. 1 A; Kang et al., 2007; Shcheglovitov et al., 2012), the exact mechanisms involved and the potential role of additional metal binding sites remain incompletely understood. Here, we have used metal ion–buffered solutions, different experimental conditions, and computational modeling to explore the effects of Zn^{2+} on $Ca_v2.3$ channel function over a wide range of free Zn^{2+} concentrations. Based on our data, we have developed a Markov model that accounts for most salient features of $Ca_v2.3$ channel gating in the absence of trace metals and also reproduces their alteration by a range of Zn^{2+} concentrations previously estimated to be (patho)physiologically relevant. In addition, our results provide novel insights into the dependence of Zn^{2+} effects on the ionic

University of Cologne, Faculty of Medicine and University Hospital Cologne, Institute for Neurophysiology, Cologne, Germany.

Correspondence to Felix Neumaier: felix@neumaier-net.de.

conditions and reveal that changes in the neuronal resting membrane potential (RMP) could profoundly influence and even invert the net Zn^{2+} action from inhibition to stimulation. Taken together, our work provides a first quantitative framework for understanding Zn^{2+} effects on $Ca_v2.3$ channel function and a step toward the application of computational approaches for understanding the complex actions of Zn^{2+} on neuronal excitability and their dependence on the prevailing neuronal properties and ionic conditions.

Materials and methods

Cell culture

Human embryonic kidney (HEK293) cells stably transfected with human $Ca_v2.3d$ and β_3 Ca^{2+}-channel subunits (Mehrke et al., 1997; Nakashima et al., 1998) were cultured under normal growth conditions (37°C and 5% CO_2) in Dulbecco's modified Eagle medium (Sigma-Aldrich) supplemented with 10% FCS and antibiotics (1% penicillin-streptomycin and selection markers; 1 mg ml^{-1} geneticin [G-418] and 200 µg ml^{-1} hygromycin B). Cells were routinely passaged twice a week using 0.05% trypsin/0.02% EDTA. For electrophysiological recordings, cells were seeded on nitric acid–washed glass coverslips and used within 24–48 h after plating.

Chemicals

HEPES (Pharmagrade), Tricine (Pharmagrade), La(III)chloride heptahydrate (99.999%), TEA chloride, Chelex 100 (sodium form), Zn(II)chloride (99.999%), pyruvic acid (98%), ATP, oxaloacetic acid, FBS, hygromycin B, geneticin, penicillin-streptomycin, hydrochloric acid (TraceSelect), and 70% nitric acid (ACS reagent) were purchased from Sigma-Aldrich. Anhydrous ethanol, diethylpyrocarbonate (high purity), sodium hydroxide 30% solution (suprapur), sodium chloride (puratronic, 99.999%; AlfaAesar), potassium chloride (puratronic, 99.997%; AlfaAesar) cesium chloride (99.999%; AlfaAesar), calcium chloride (99.99%; AlfaAesar), 50% cesium hydroxide solution (99.9%; AlfaAesar), D-glucose (AnalaR Normapur), and potassium hydroxide (99.98%) were purchased from VWR. 1,000 mM stock solutions of diethyl pyrocarbonate (DEPC) in anhydrous ethanol were prepared on the day of the experiments, kept on ice, and diluted into standard external solution immediately before use.

Preparation of buffered Zn^{2+} solutions

To avoid trace metal contamination and reduce uncertainties with regard to free metal ion concentrations in our recording solutions, we employed suitable labware and sample handling procedures, which have been outlined in detail in a previous publication (Neumaier et al., 2017). Briefly, all solutions were prepared using type 1 ultrapure water (Purelab Flex 2 by ELGA Labwater), metal-free pipette tips, and reagents of the highest purity available (see previous section). All containers used for preparation and storage were made from polymethylpentene, polystyrene, or low-density polyethylene and pretreated by a comprehensive cleaning procedure that involved rinses with alcohol, successive soaking in dilute (10%) hydrochloric and nitric acid, and extensive washes with type 1 ultrapure water. Before the addition of multivalent cations or chelators, all solutions were treated with the metal-chelating ion exchange resin Chelex 100 to remove adventitious metal ions. For most experiments, Tricine (10 mM) was used as a dual proton and metal ion buffer to prepare buffered Zn^{2+} solutions (solutions 1–3A in Table S1). Free Zn^{2+} concentrations above the useful range for buffering with Tricine were prepared in a HEPES-buffered background solution (solutions 1–3B in Table S1). There was no difference in the electrophysiological properties recorded in Tricine- versus HEPES-buffered solutions, suggesting that our methods were sufficient to reduce trace metal contamination below the limits for detection. To facilitate fast and complete reversal of metal ion effects during washout, however, the HEPES-buffered solution used for control recordings and washout was supplemented with 0.1 mM of the trace metal chelator diethylenetriaminepentaacetic acid. In all cases, pH-, temperature-, and ionic strength–corrected free metal ion concentrations were calculated with the general-purpose speciation software Visual MINTEQ and constants reported previously (Mohamed, 2007; Goldberg et al., 2002; Khalil et al., 2009). Apart from Zn^{2+} binding by Tricine, these calculations took into account the formation of hydroxide species and the (weak) binding by Tricine of Ca^{2+} ions so as to ensure that the estimated free Ca^{2+} concentration was the same in HEPES- and Tricine-buffered solutions.

Ionic and gating current recordings

Cells were voltage clamped using the whole-cell configuration of the patch-clamp technique (Hamill et al., 1981). Pipettes were prepared from thick-walled borosilicate glass capillaries (1.5/0.84 mm OD/ID; World Precision Instruments) using a P97 Micropipette puller (Sutter Instruments). Resistance of the resulting electrodes was between 1.5 and 6.5 MΩ when filled with standard internal solution. The bath was connected to ground via 140 mM sodium chloride agar bridges. Currents were sampled at 20 or 50 kHz and filtered at 10 kHz using an EPC9 amplifier (HEKA) controlled with HEKA's Pulse software. Leak and capacitive currents were subtracted online using a −P/5 (for ionic currents) or −P/8 (for gating currents) protocol. Series resistance was compensated electronically by ≤90% and continuously monitored throughout the measurements. All experiments were performed at room temperature (20–22°C) and, unless noted otherwise, from a holding potential of −80 mV for ionic current recordings or −100 mV for gating current recordings. During the experiments, cells were constantly perfused with external solution at a rate of ∼2–4 ml min^{-1} using a gravity-driven perfusion system controlled by manual precision flow regulators (Sarstedt). The standard external solution for ionic current recordings contained (in mM) 120 NaCl, 5 KCl, 20 TEA chloride, 10 D-glucose, 10 Tricine, and 2.8/5.8 $CaCl_2$ or 10 HEPES and 2.3/4.5 $CaCl_2$ (= 2/4 mM free Ca^{2+}; for details, see Table S1) with the pH adjusted to 7.4 using NaOH or HCl and osmolarity of 297–314 mOsm. Gating currents were recorded in the same HEPES-buffered solution but with 4 mM free $MgCl_2$ (instead of $CaCl_2$) and 0.1 mM free La^{3+} (0.2 mM $LaCl_3$ + 0.1 mM EDTA) to block ionic currents. Ca^{2+} substitution by Mg^{2+} did not alter channel voltage dependence (Fig. S1 A), whereas 100 µM

free La^{3+} shifted it by 8.3 ± 0.7 mV (n = 6 cells) to more depolarized test potentials (Fig. S1 B), which was taken into account by assuming a 10-mV shift during fitting.

The standard internal solution was composed of (in mM) 130 CsCl, 5 oxaloacetic acid, 5 creatine, 5 pyruvic acid, 10 EGTA, 10 HEPES, and 4 MgATP with the pH adjusted to 7.3 using CsOH and osmolarity of 275–295 mOsm. It was filtered through 0.2-µm surfactant-free cellulose acetate membranes (Corning) and kept on ice between the recordings. The liquid junction potential between internal and external solution (calculated using the JPcalc algorithm in pClamp 10; Molecular Devices) was ∼5 mV. Since no correction for the liquid junction potential was done, all voltages shown were actually 5 mV more negative.

Whole-cell protocols

During the experiments, currents were routinely monitored by application at 0.03 Hz of a 30-ms test pulse to +10 mV followed by 10-ms repolarization at −50 mV to record well-resolved tail currents. To construct steady-state I-V relationships, peak currents recorded with a protocol consisting of 25-ms test pulses to potentials between −80 mV and +60 mV (10-mV increments at 0.1 Hz) were normalized by the cell capacitance or maximum current amplitude under control conditions and plotted as a function of the test-pulse potential. Tail-current amplitudes recorded during repolarization to −50 mV at the end of the voltage steps were normalized to the maximum tail-current amplitude and plotted as a function of the prepulse potential to construct isochronous activation curves. Gating currents were recorded with the same protocol, except that the holding potential was −100 mV, the test pulse duration was reduced to 20 ms, and repolarization was also to −100 mV.

Instantaneous I-V (II-V) relationships were obtained with a protocol consisting of a fixed 10-ms prepulse to +60 mV followed by 40-ms test pulses to potentials between −80 mV and +60 mV (10-mV increments at 0.1 Hz). Instantaneous (tail) current amplitudes recorded during the test pulses were normalized by the cell capacitance or maximum tail current amplitude under control conditions and plotted as a function of the test-pulse potential.

The fraction of channels available for activation from different holding potentials was assessed by a protocol consisting of 2-s conditioning prepulses at potentials between −120 mV and +10 mV (10-mV increments at 0.1 Hz) followed by a fixed 35-ms test pulse to +10 mV. To construct prepulse inactivation (PPI) curves, peak current amplitudes recorded during the test pulse were normalized by the maximum amplitude and plotted as a function of the prepulse potential.

Data analysis and statistics

Leak-subtracted current traces were directly analyzed with PulseFit (HEKA) or exported for further processing with Microsoft Excel 2010 and OriginLab Pro (version 9; OriginLab).

I-V relationships were fitted with a combined Ohm–Boltzmann equation:

$$I = (V_m - V_{rev}) \times G_{max} / \{1 + \exp[-(V_m - V_{0.5})/k]\}, \quad (1)$$

where I is the (normalized) peak current density measured at the test potential V_m, V_{rev} the apparent reversal potential, G_{max} the maximum slope conductance, $V_{0.5}$ the voltage eliciting half-maximal inward currents, and k the slope factor. Isochronous activation and PPI curves were fitted with single Boltzmann equations:

$$I/I_{max} = A_2 + (A_1 - A_2)/\{1 + \exp[(V_m - V_{0.5})/k]\}, \quad (2)$$

where I/I_{max} is the normalized current corresponding to the prepulse potential V_m, $V_{0.5}$ is the voltage of half-maximal activation ($V_{0.5act}$) or inactivation ($V_{0.5inact}$), k the activation (k_{act}) or inactivation (k_{inact}) slope factor, and A_1 and A_2 the initial and final values, respectively. Activation time constants were determined by single exponential functions fit to the rising phase of currents, which started when the current amplitude had reached 20% of its final value. Inactivation during 400-ms voltage steps was biexponential, but the slower time constant was often too slow to be determined reliably (τ_{slow} > 200–700 ms depending on the test potential), so that inactivation time constants were determined using a single exponential function with variable offset fitted to the decaying phase of currents. Tail current decay over a wide voltage range was quantified by the sum of up to three exponential functions, where the two faster time constants presumably reflect deactivation and the third, slowest time constant corresponds to inactivation. Weighted deactivation time constants were calculated according to the following equation:

$$\tau_w = (A_1 \times \tau_1 + A_2 \times \tau_2)/(A_1 + A_2), \quad (3)$$

where τ_w is the weighted time-constant, A_1 and τ_1 are the relative amplitude and time-constant of the first exponential component and A_2 and τ_2 the relative amplitude and time-constant of the second exponential component. All fits were performed using the Levenberg-Marquardt least-squares algorithm and the goodness of fits was judged based on residual plots and adjusted χ^2 values. Smooth curves in the figures represent fits to average data whereas values given in the text are average data from fits to individual measurements. Values in the text and figures are expressed as mean ± SEM based on n, the number of independent experiments. Boxplots show median, upper and lower quartiles (box), minimum and maximum values (whiskers), and individual data points (dots). Numerical values for the parameters characterizing monotonic concentration-response curves were obtained from fits of the data with a standard sigmoid saturation curve of the form:

$$Y = A_1 + (A_2 - A_1) \Big/ \left\{1 + 10^{[(\log K_{Zn} - X) \times h]}\right\}, \quad (4a)$$

where X is the logarithm of the free Zn^{2+} concentration that produces the effect Y, A_1 is the bottom asymptote, A_2 the top asymptote or maximum effect (E_{max}), K_{Zn} the free Zn^{2+} concentration producing 50% of the E_{max} (= apparent dissociation constant for Zn^{2+}), and h the Hill slope. Biphasic concentration–response curves were fitted with a combination of two sigmoid saturation curves of the form

$$Y = A_1 + (A_2 - A_1)\left\{\frac{p}{1 + 10^{[(\log K_{Zn1} - X) \times h1]}} + \frac{1 - p}{1 + 10^{[(\log K_{Zn2} - X) \times h2]}}\right\}, \quad (4b)$$

where X is the logarithm of the free Zn^{2+} concentration that produces the effect Y, A_1 and A_2 are the bottom and top

asymptotes, K_{Zn1} and K_{Zn2} the free Zn^{2+} concentrations producing 50% of the E_{max} is mediated by the two components, h_1 and h_2 the corresponding Hill slopes, and p the proportion of maximum response due to the more potent component. Unless noted otherwise, the Hill slopes were fixed to 1 (but see Limitations).

To indicate experimental uncertainty, we assumed a Gaussian distribution of the fit parameters and used 84% confidence intervals (CIs), so that the probability that two CIs abut or overlap if there really is no difference should be roughly equal to or smaller than P = 0.05, respectively (Austin and Hux, 2002). In all other cases, statistical significance was assessed with OriginLab Pro 9 using a repeated-measures ANOVA followed by Bonferroni's post hoc analysis when comparing mean values from the same cells or a one-way ANOVA followed by Bonferroni's post hoc analysis when comparing multiple independent mean values. Homogeneity of variances between groups was tested using Levene's test for equality of variances on the squared deviations. In the case of heteroscedastic data ($P < 0.05$ in Levene's test and ratio of largest to smallest variance ≥4), statistical significance was assessed with Minitab (version 17; Minitab) using Welch's ANOVA and the Games-Howell multiple comparison method.

Modeling and simulations

Model development, optimization, and simulations were performed using the NEURON version 7.6.2 simulation environment (Carnevale and Hines, 2006). Kinetic equations were written and solved directly using KINETIC methods of the NMODL language in NEURON.

The rates of Zn^{2+} interaction with different sites were defined in terms of a simple, bimolecular reaction:

$$k_{on} = [Zn] \times d_{Zn} \quad (5a)$$

and

$$k_{off} = d_{Zn} \times K_{Zn}, \quad (5b)$$

where [Zn] is the free Zn^{2+} concentration, d_{Zn} is the rate of complex formation between Zn^{2+} and the site, and K_{Zn} is the affinity of the site for Zn^{2+}.

For parameter optimization and whole-cell simulations, we constructed an in silico one-compartmental model of a HEK293 cell with diameter and length of 21.851 µm, which corresponds to a sphere with surface area of 1,500 µm². Temperature, specific membrane capacitance, and cytoplasmic resistivity were set to 22°C, 1 µF/cm², and 60 Ω×cm, respectively. All simulations were performed using the default integration strategy with an implicit fixed time step of 25 µs.

For kinetic modeling, mean current traces (in pA/pF) were calculated from all control recordings performed with the voltage protocols shown in Fig. 15, C–F and converted to mA/cm² assuming a specific membrane capacitance of 1 µF/cm². The model shown in Fig. 15 A was then simultaneously fitted to the whole set of experimental traces using the nonlinear least-squares minimization method included in NEURON (Multiple Run Fitter [MRF] subroutine), which is based on the principal axis method described by Brent (1976). Approximately equal weighting of current traces recorded with different protocols was achieved by scaling the error values reported by each MRF generator until it was close to the value reported by all other MRF generators.

Macroscopic ion currents (in mA/cm²) were calculated according to

$$I_{ion} = P_o \times n \times p \times ghk(V_m, Ca_i, Ca_o), \quad (6)$$

where P_O is the faction of channels in the four open states, n is the number of channels per square centimeter, p is the single-channel permeability, and ghk is the Goldman–Hodgkin–Katz current equation. The single-channel permeability was assumed to be 7.5×10^{-14} cm^3s^{-1}, and the number of channels per square centimeter was set to values between 1.15×10^{10} and 1.40×10^{10} to account for differences in expression levels between experiments performed with the different voltage protocols.

Macroscopic gating currents were calculated as the product of the number of channels and the sum, over all pairs of states, of the charge movement between states times the fraction of channels in each state times the transition rate between the states. Some of the optimizations were run on the Neuroscience Gateway (Sivagnanam et al., 2013). Source code for the model reported in this paper and several scripts for running simulations are available in ModelDB (McDougal et al., 2017) at http://modeldb.yale.edu/261714.

Online supplemental material

Fig. S1 shows the effects of Ca^{2+} substitution with Mg^{2+} or 100 µM free La^{3+} on $Ca_v2.3$ channel voltage dependence. Fig. S2 shows evidence for fast and slow components of charge movement observed in our gating current recordings. Fig. S3 compares experimental and simulated $Ca_v2.3$ channel biophysical properties in the absence of metal ions. Table S1 lists the composition of all external solutions used in the electrophysiological recordings. Table S2 presents the absolute effects of 5.4 µm free Zn^{2+} on $Ca_v2.3$ channel gating under different experimental conditions. Table S3 lists the relative effects of vatious free Zn^{2+} concentrations on $Ca_v2.3$ channel gating under different experimental conditions. Table S4 shows E_{max} and K_{Zn} values obtained from Zn^{2+} concentration-response data under different experimental conditions. Table S5 shows global K_{Zn} values for high-affinity shift and slowing.

Results

We reassessed the action of Zn^{2+} on $Ca_v2.3$ channel function under near-physiological ionic conditions with either 2 or 4 mM free Ca^{2+} as the charge carrier and at two different pH values. To identify gating effects caused by binding to the putative metal binding site in domain I, some recordings were performed after carbethoxylation of extracellular histidine residues with DEPC (Fig. 1 B). Unless noted otherwise, all recordings were performed at room temperature (20–22°C) and from a holding potential of −80 mV. The key electrophysiological properties as a function of the experimental conditions in the absence of Zn^{2+} or other trace metals (control recordings with Tricine or HEPES + diethylenetriaminepentaacetic acid) are summarized in Table 1. In the

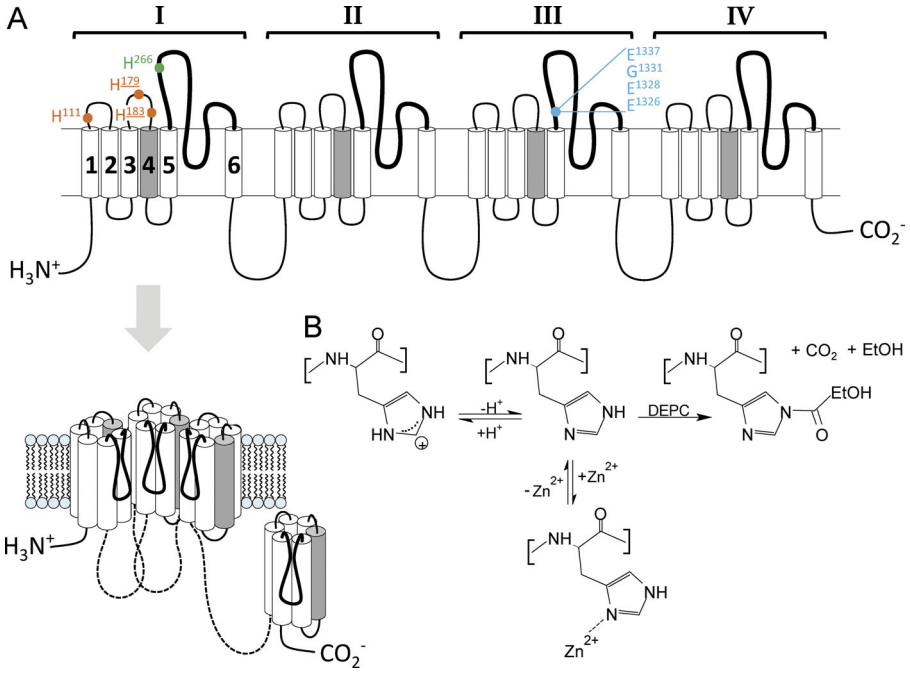

Figure 1. **General structure and potential Zn^{2+}-binding sites in $Ca_v2.3$ channels. (A)** General structure and transmembrane topology of $Ca_v2.3$ channels along with residues that have been implicated in the effects of Zn^{2+} and/or protons. Three nonconserved histidine residues in domain I (indicated in orange) have been linked to gating modulation by Zn^{2+}, other d-block metal ions, and (for underlined residues) protons (Cens et al., 2011; Shcheglovitov et al., 2012; Kang et al., 2007). A nonconserved histidine residue in the p-loop of domain I (indicated in green) has been linked to proton-induced changes in single-channel conductance (Cens et al., 2011). An EF hand–like motif in the S5-H5 region of domain III (indicated in light blue) that is present in all HVA channels has been implicated in their differential sensitivity to Zn^{2+} (Sun et al., 2007). **(B)** Scheme illustrating possible reactions of histidine residues with protons (left), Zn^{2+} ions (bottom), or DEPC (right).

first part of the Results, we will briefly describe the hallmarks of $Ca_v2.3$ channel modulation by low micromolar Zn^{2+} levels and their dependence on time, voltage, ionic conditions, and Zn^{2+} interaction with histidine residues. In the second and third parts, we will summarize their rather complex dependence on Zn^{2+} concentration and try to delineate effects mediated by high- and low-affinity binding. The fourth part briefly describes the development of a model for $Ca_v2.3$ channel gating in the absence of trace metals, while the last part deals with our approach to model the major Zn^{2+} effects on $Ca_v2.3$ channel gating.

$Ca_v2.3$ channel modulation by low micromolar Zn^{2+} concentrations

Fig. 2 exemplifies the effects of 5.4 µM Zn^{2+} on macroscopic currents carried by 4 mM free Ca^{2+} at pH 7.4. Currents were evoked by step depolarization to different test potentials and repolarization to −50 mV (Fig. 2 A, I-V protocol), a fixed test pulse following 2-s prepulses at different conditioning potentials (Fig. 2 B, PPI protocol), or repolarization to different test potentials following a fixed depolarizing prepulse to open the channels (Fig. 2 C, II-V protocol). Zn^{2+}-induced suppression was strong and steeply voltage dependent when recorded with the I-V protocol, as reflected in a shift of the I-V curve to more depolarized test potentials (Fig. 2, A and D). The same concentration of Zn^{2+} produced almost no changes in currents measured with the II-V protocol (Fig. 2, C and E).

Zn^{2+} shifts and alters channel voltage dependence

Fig. 2 F shows isochronous activation and inactivation curves, constructed from tail currents recorded with the I-V protocol or from the fraction of current available for activation recorded with the PPI protocol, respectively. Application of 5.4 µM Zn^{2+} produced a depolarizing shift of both activation and inactivation voltage dependence by almost 10 mV (Fig. 2 G), which was completely reversed during washout with Zn^{2+}-free solution (Fig. 2 F). The shift was paralleled by a decreased slope of the activation curve, as reflected in a moderate but significant and selective increase of the activation slope factor by ∼10–15% (Fig. 2 H).

Zn^{2+} slows macroscopic current kinetics

Apart from altering channel voltage dependence, Zn^{2+} produced a dramatic slowing of current kinetics that is most evident when inspecting scaled I-V current traces (Fig. 3 A). Fig. 4 A summarizes the effects of 5.4 µM Zn^{2+} on the time course of macroscopic activation (right) and deactivation (left) at various test potentials, quantified by fitting exponential functions to the rising phase of I-V currents (Fig. 2 A and Fig. 3 A) or the decaying phase of II-V currents (Fig. 2 C and Fig. 3 B), respectively. It can be seen that the effects on activation kinetics were much more pronounced than would be expected based on the voltage shift described above. Thus, after correction for the expected effects of a 10-mV shift on activation kinetics, 5.4 µM Zn^{2+} still slowed current activation almost twofold and over the whole voltage range examined.

On the other hand, Zn^{2+} had no effects on deactivation time constants except for a minor increase at intermediate test potentials (Fig. 4 A), which could reflect the depolarizing shift in channel voltage dependence. Interestingly, inspection of scaled II-V current traces near the threshold voltage for macroscopic activation still revealed a clear acceleration of tail-current decay (Fig. 3 B), which was related to neither changes in deactivation time constants nor faster inactivation (Fig. 4 B). Instead, the faster tail-current decay in the presence of Zn^{2+} appeared to result almost entirely from a depolarizing shift in the relative amplitude of both processes, which markedly increased the apparent contribution of deactivation to total tail-current decay at depolarized test potentials (Fig. 4 C). Indeed, when the time

Table 1. **Electrophysiological properties of $Ca_v2.3$ channels in the absence of metal ions**

	$V_{0.5act}$ [mV]	k_{act}	*n*	$\tau_{act(10\ mV)}$ [ms]	$\tau_{deact(-50\ mV)}$ [ms]	*n*
4 Ca, pH 7.4	−2.3 ± 0.3	6.8 ± 0.1	87	1.3 ± 0.1	0.38 ± 0.01	95
4 Ca, pH 7.0	−0.2 ± 0.4[a]	6.6 ± 0.1	51	1.6 ± 0.1[b]	0.40 ± 0.01	66
2 Ca, pH 7.4	−3.1 ± 0.4	7.7 ± 0.2[a]	37	1.3 ± 0.1	0.37 ± 0.01	63
4 Ca, pH 7.4 (DEPC)	−11.4 ± 0.8[a]	8.7 ± 0.3[a]	34	1.1 ± 0.1[c]	0.42 ± 0.01	63

[a]P < 0.001 versus 4 Ca, pH 7.4 (Welch ANOVA and Games-Howell analysis).
[b]P < 0.05 versus 4 Ca, pH 7.4 (Welch ANOVA and Games-Howell analysis).
[c]P < 0.01 versus 4 Ca, pH 7.4 (Welch ANOVA and Games-Howell analysis).

course of inactivation was examined using 400-ms voltage steps, Zn^{2+} actually slowed down both fast and slow components of current decay recorded near the half-activation voltage (Fig. 3 A). However, there was no effect on the limiting decay rate reached at depolarized test potentials (Fig. 4 D) or on the time constants for recovery from inactivation at −80 mV (data not shown), suggesting that the underlying microscopic inactivation rates were unaffected. Because macroscopic inactivation is thought to derive most of its voltage dependence from the voltage dependence of activation, the observed shift in inactivation voltage dependence might have been a consequence of the Zn^{2+}-induced changes in activation gating (but see Modeling the effects of Zn^{2+} on $Ca_v2.3$ channel gating).

Zn^{2+} effects depend on the holding potential

Regardless of the underlying mechanism, the shift of the inactivation curve (Fig. 2 F) suggested that Zn^{2+} increases the availability for activation after prepulses at intermediate test potentials, in which case its effects could be influenced by the RMP. To test this assumption, we compared the effects of Zn^{2+} on currents evoked by step depolarization from different holding potentials. As illustrated in Fig. 5, Ca^{2+} currents evoked from voltages that provide full availability (i.e., less than or equal to −80 mV) were rapidly inhibited and slowed by application of 5.4 µM free Zn^{2+} and quickly returned to their control amplitude and kinetics during washout (Fig. 5, A, B, and D), indicating that Zn^{2+} application and washout were complete in <30 s. Currents

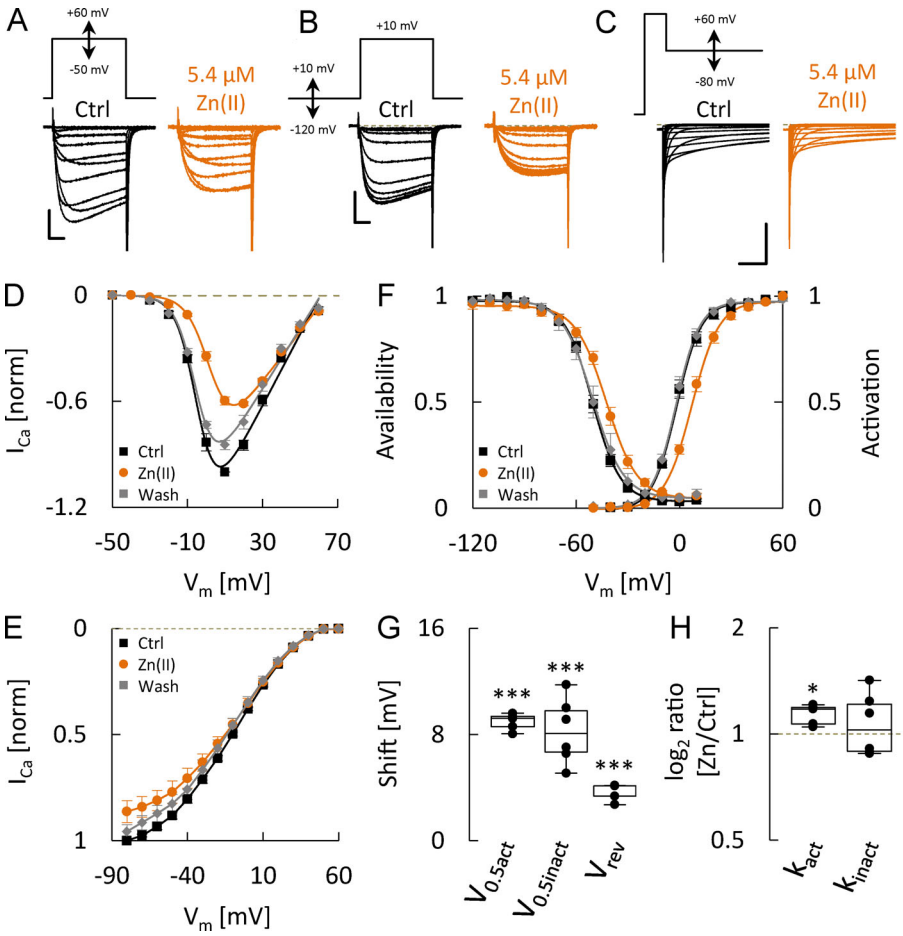

Figure 2. **Effects of Zn^{2+} on $Ca_v2.3$ channel voltage dependence. (A–C)** Families of mean current traces carried by 4 mM free Ca^{2+} and recorded with the protocols depicted above in the absence (black) and presence (orange) of 5.4 µM free Zn^{2+} at pH 7.4 (*n* = 5 cells in A and C, and 6 cells in B). Scale bar corresponds to 5 ms and 20 pA/pF in A, 5 ms and 50 pA/pF in B, or 10 ms and 200 pA/pF in C. **(D)** I-V relationships determined with the protocol in A before (black squares), during (orange circles), and after (gray diamonds) application of 5.4 µM free Zn^{2+} (same cells as in A). **(E)** II-V relationships determined with the protocol in C before (black squares), during (orange circles), and after (gray diamonds) application of 5.4 µM free Zn^{2+} (same cells as in C). **(F)** Isochronous activation (right) and PPI (left) curves determined from tail currents recorded with the protocol in A or peak currents recorded with the protocol in B, respectively, before (open squares), during (orange circles), and after (gray squares) application of 5.4 µM free Zn^{2+} (same cells as in A and B). **(G)** Boxplots comparing the Zn^{2+}-induced shifts in half-activation voltage ($V_{0.5act}$), half-inactivation voltage ($V_{0.5inact}$), and apparent V_{rev}. **(H)** Boxplots comparing the Zn^{2+}-induced changes in activation slope factor (k_{act}) and inactivation slope factor (k_{inact}). *, P < 0.05; ***, P < 0.001 (one-way repeated-measures ANOVA).

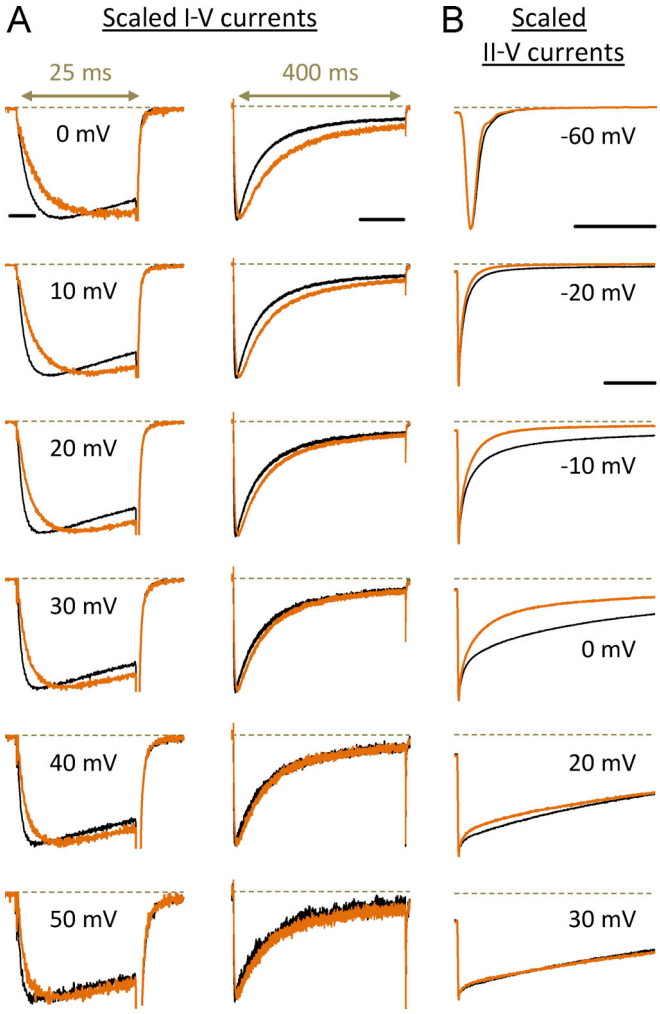

Figure 3. **Effects of Zn^{2+} on the shape of macroscopic Ca^{2+} currents.** **(A)** Mean I-V current traces recorded in response to 25-ms (left) or 400-ms (right) voltage steps to the indicated test potentials in the absence (black) and presence (orange) of 5.4 µM free Zn^{2+} at pH 7.4. They have been scaled to their maximum amplitude to highlight kinetic changes. Scale bars correspond to 10 and 100 ms for short and long voltage steps, respectively. **(B)** Mean II-V current traces recorded at the indicated test potentials in the absence (black) and presence (orange) of 5.4 µM free Zn^{2+} at pH 7.4. They have been scaled to their maximum amplitude to highlight kinetic changes. Scale bars correspond to 2 ms for the tail current at −60 mV and 10 ms for all other test potentials.

evoked from more depolarized holding potentials displayed the same rapid slowing, but suppression was diminished and followed by a paradoxical increase of current amplitudes in the maintained presence of Zn^{2+} (Fig. 5 A), during which the kinetic slowing persisted (Fig. 5 B). For example, currents evoked from a holding potential of −60 mV were reduced to 85 ± 3% of their initial amplitude 30 s after application of 5.4 µM Zn^{2+} but then progressively increased to reach a steady-state level at 128 ± 7% of their control amplitude after 240 s in the maintained presence of Zn^{2+} (Fig. 5, A and C). Subsequent washout of Zn^{2+} rapidly restored the normal activation kinetics (Fig. 5 B) and led to overrecovery of current amplitudes beyond their initial level, which was followed by a gradual return toward the control amplitude. The same but less pronounced effects were observed when the free Zn^{2+} concentration was reduced to 2.3 µM (data not shown). In principle, Zn^{2+}-induced stimulation that gets evident as the holding potential becomes more depolarized would be consistent with a shift in the voltage dependence of inactivation, which should increase availability near the voltage of half-maximal inactivation. However, considering the slow time course of current increase, most of the observed stimulation could not be explained by the increase in availability measured after 2-s prepulses. To roughly separate the two opposing effects of Zn^{2+}, the difference in peak current amplitudes between the last test pulse delivered in the presence of Zn^{2+} and the first test pulse delivered after starting washout was taken as a measure for the degree of Zn^{2+}-induced suppression and used to correct the original peak current amplitudes measured in the presence of Zn^{2+}. Fig. 6 A illustrates the magnitude and time course of current stimulation thus obtained at different holding potentials (top) and also indicates the estimated magnitude of suppression (bottom), which showed no dependence on holding potential. Fig. 6 B compares the current increase after 240 s in the presence of Zn^{2+} from Fig. 6 A with the increase in availability determined using the PPI protocol. Both effects exhibited the bell-shaped voltage dependence that would be expected for a shift in inactivation, but the slow changes peaked at ∼30 mV more negative holding potentials. A possible explanation for these findings could be that Zn^{2+} also shifts a process like ultraslow voltage-dependent inactivation, which occurs at more negative holding potentials and with time constants for development and recovery in the order of minutes (Boyett et al., 1994; Yasuda et al., 2004). True steady-state inactivation curves that reflect such processes could not be obtained, as the long prepulse durations necessary were neither practical nor tolerated by the cells. However, a testable prediction of the above assumption is that the time course of recovery from inactivation produced by a hyperpolarizing shift in holding potential equivalent to the Zn^{2+}-induced depolarizing shift in activation voltage dependence should roughly match that of Zn^{2+}-induced stimulation at the same holding potential. Fig. 6 C shows data from a recording where the holding potential was changed from −60 mV to −70 mV and back to −60 mV as indicated. Neither the time course (Fig. 6 D) nor the degree (Fig. 6 E) of current increase were significantly different from the values for Zn^{2+}-induced stimulation at the same holding potential, suggesting that the latter effect was also due to slow recovery from holding potential–dependent inactivation.

Zn^{2+} effects depend on histidine residues

Previous studies have linked both pH- and metal-induced changes in $Ca_v2.3$ channel gating to histidine residues making up the proposed metal binding site in domain I (Fig. 1 A; Cens et al., 2011; Kang et al., 2007; Shcheglovitov et al., 2012). Because divalent cations often compete with each other and protons for binding to the histidine imidazole ring, one of our aims was to assess how changes in the ionic conditions or histidine modification influence Zn^{2+}-induced modulation. As illustrated in Fig. 7, A–D and Table S2, reducing the concentration of Ca^{2+} (from 4 to 2 mM) or moderate acidification

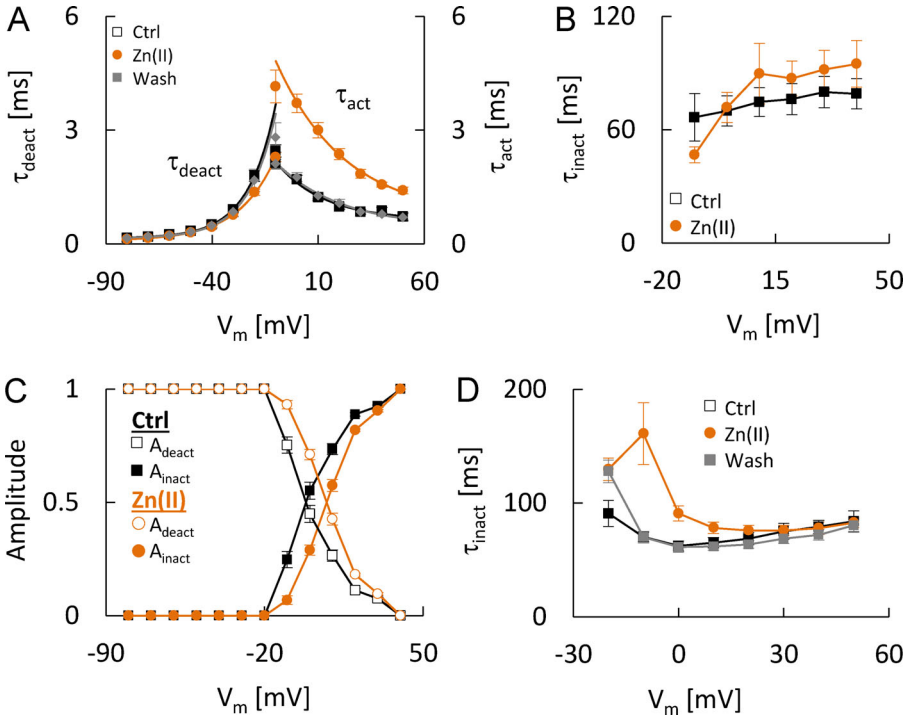

Figure 4. **Effects of Zn^{2+} on macroscopic activation, deactivation, and inactivation kinetics. (A)** Activation (right) and deactivation (left) time-constants, determined from exponential fits to I-V or II-V currents carried by 4 mM free Ca^{2+} and recorded before (black squares), during (orange circles), and after (gray diamonds) application of 5.4 µM free Zn^{2+} at pH = 7.4. Note that deactivation time-constants reflect a weighted τ comprising fast and intermediate components of tail-current decay. **(B)** Inactivation time constants determined from exponential fits to II-V current decay at the indicated test potentials in the absence (black squares) and presence (orange circles) of 5.4 µM Zn^{2+} (same cells as in A). **(C)** Contribution of deactivation (open symbols) and inactivation (filled symbols) to total II-V current decay in the absence (black squares) and presence (orange circles) of 5.4 µM Zn^{2+} (same cells as in A and B). **(D)** Inactivation time constants, determined from exponential fits to the decaying phase of currents recorded during 400-ms voltage steps to the indicated test potentials before (open squares), during (orange circles), and after (gray squares) application of 5.4 µM Zn^{2+}.

(from pH 7.4 to 7.0) significantly increased or decreased, respectively, the changes in activation voltage dependence and kinetics produced by 5.4 µM Zn^{2+}, suggesting that Ca^{2+} and protons both counteract the effects of Zn^{2+} on gating. The pH reduction also significantly slowed and shifted activation under control conditions (Table 1), indicating that protonation of residues in the Zn^{2+} site could produce gating effects similar to Zn^{2+} binding.

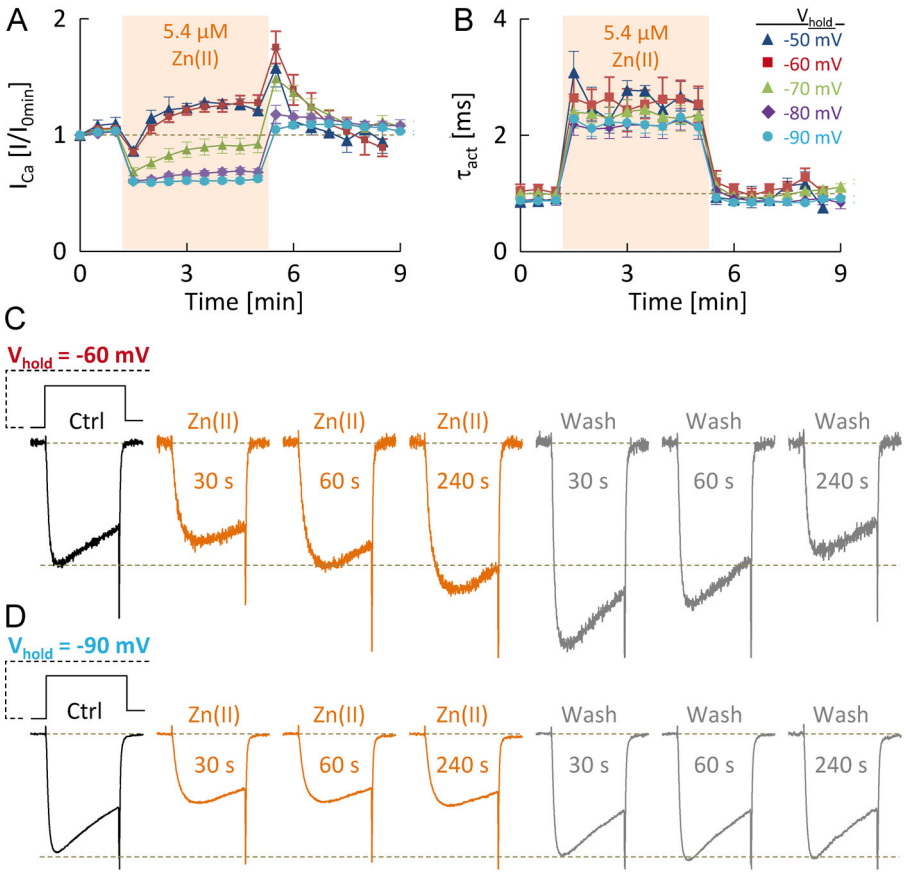

Figure 5. **Kinetics of Zn^{2+}-induced modulation at different holding potentials. (A)** Time course of Zn^{2+}-induced changes in peak currents carried by 4 mM free Ca^{2+} and evoked by voltage steps to 10 mV from the indicated holding potentials (n = 6–9 cells per holding potential). **(B)** Time course of Zn^{2+}-induced changes in activation time constants determined in the same cells as in A. **(C)** Mean current traces recorded at the indicated time points before, during, and after Zn^{2+}-application from a holding-potential of −60 mV (n = 8 cells). **(D)** Mean current traces recorded as in B but from a holding potential of −90 mV (n = 8 cells).

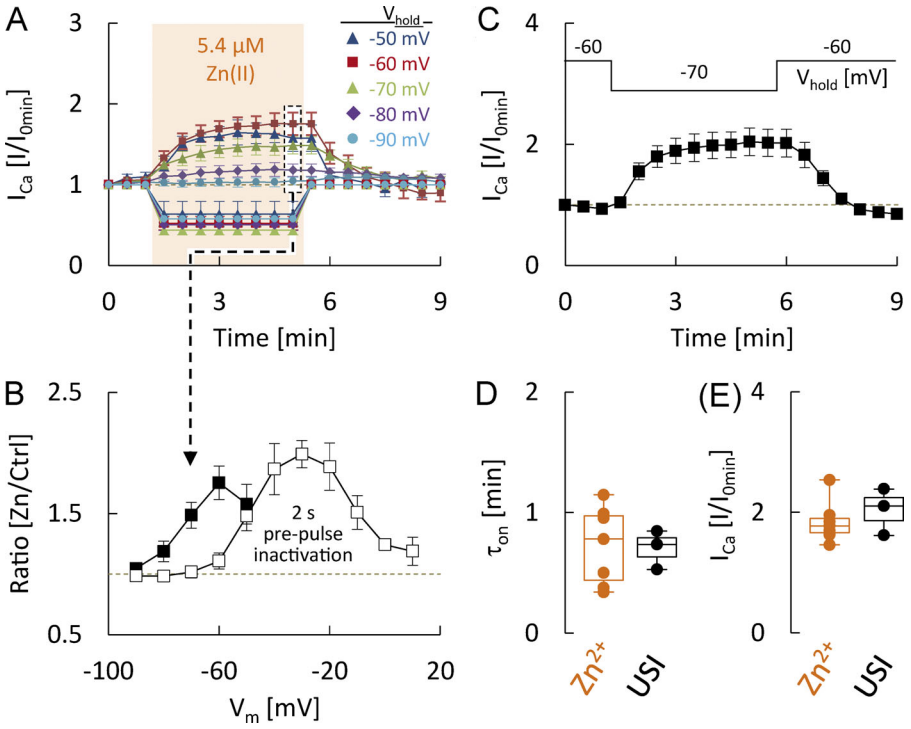

Figure 6. **Zn^{2+}-induced stimulation and the role of ultraslow inactivation gating. (A)** Time course and degree of stimulation (top) and suppression (bottom) during application of 5.4 µM free Zn^{2+} at different holding potentials after separation of the opposing effects as described in the text (same cells as in Fig. 5). **(B)** Comparison of the relative Zn^{2+}-induced increase of currents at 10 mV determined from the data in Fig. 2 F (i.e., after 2-s prepulses at the indicated test potentials, open squares) or A (i.e., 240 s after addition of Zn^{2+} at the indicated holding potentials, black squares). **(C)** Slow holding potential–dependent recovery from and development of inactivation induced by switching the holding potential from −60 mV to −70 mV and back to −60 mV in the absence of trace metal ions (n = 3 cells). **(D)** Comparison of time constants determined by exponential fits to the development of Zn^{2+}-induced stimulation at a holding potential of −60 mV in A (Zn^{2+}, orange) or to the recovery from holding potential-dependent inactivation in C (USI, black). **(E)** Comparison of the magnitude of current increase during Zn^{2+}-induced stimulation at a holding potential of −60 mV (Zn^{2+}, orange) and during recovery from holding potential–dependent inactivation (USI; black).

Pretreatment with the histidine-modifying agent DEPC almost completely prevented the Zn^{2+}-induced shift (Fig. 7 C) and slowing (Fig. 7, B and D), confirming that both effects are related to interaction with histidine residues, presumably located in the proposed metal ion binding site. In addition, DEPC produced gating effects opposite to those exerted by Zn^{2+} and selectively stimulated $Ca_v2.3$ channel activation in the absence of trace metal ions, as reflected in a significant shift of the activation curve by ∼9 mV toward more negative test potentials and accelerated activation kinetics under control conditions (Table 1).

Finally, DEPC pretreatment also prevented the Zn^{2+}-induced increase of the activation slope factor (Fig. 7 E), but several observations indicated that the underlying mechanism may differ from that mediating the shift and slowing. First, pH reduction reproduced the other gating effects of Zn^{2+} as described above but had no effect on the slope of the activation curve

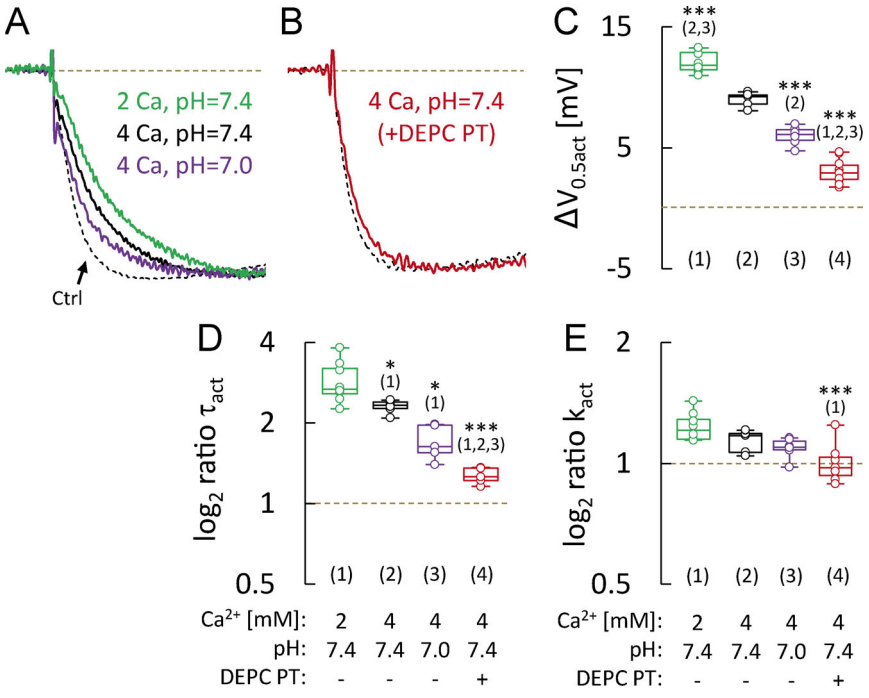

Figure 7. **Dependence of Zn^{2+} effects on extracellular Ca^{2+} concentration, pH, and histidine residues. (A–E)** Comparison of normalized mean current traces (A and B) and changes in half-activation voltage ($V_{0.5act}$; C), activation time constants at 10 mV (τ_{act}; D), and activation slope factor (k_{act}; E) produced by application of 5.4 µM free Zn^{2+} under the experimental conditions indicated below (n = 5–8 cells per experimental condition). *, P < 0.05; ***, P < 0.001 (one-way ANOVA with Bonferroni post hoc test). DEPC PT, DEPC pretreatment.

under control conditions (Table 1). Second, manipulation of the Ca^{2+} concentration or of the pH of the extracellular solution significantly altered the other gating effects of Zn^{2+} (Fig. 7, A–D) but had no effect on the Zn^{2+}-induced changes in k_{act} (Fig. 7 E). Third, while DEPC pretreatment produced effects opposite to the shift and slowing, it reproduced Zn^{2+}-induced changes in the slope of the activation curve, as reflected in a significant increase of k_{act} in pretreated cells under control conditions (Table 1).

Concentration dependence of Zn^{2+}-induced gating changes

To further corroborate and extent the above findings, we performed additional experiments with a wide range of free Zn^{2+} levels. Fig. 8 A, Fig. 9 A, and Fig. 10 A show concentration–response curves, which were constructed by plotting the indicated Zn^{2+}-induced gating changes as a function of the logarithm of the free Zn^{2+} concentration and fitted with one (Eq. 4a) or a combination of two (Eq. 4b) sigmoid saturation curves. Best-fit values and CIs for apparent dissociation constants (K_{Zn}) and E_{max} values obtained under the different experimental conditions are summarized below each plot (Fig. 8, B and C; Fig. 9, B and C; and Fig. 10, B and C) and in Table S4.

Micromolar Zn^{2+} concentrations slow and shift by multiple mechanisms

The concentration–response curves for the Zn^{2+}-induced shift in activation voltage dependence were clearly biphasic under all experimental conditions examined, revealing the existence of two separable components with vastly different affinities (Fig. 8). They could be well described by a combination of two simple saturation curves with Hill slopes of 1 (Eq. 4b), indicating that Zn^{2+} may exert its effects through interaction with at least two independent sites. The concentration dependence for changes in inactivation voltage dependence (not shown, but see Table S4) and for the (shift-corrected) Zn^{2+}-induced slowing (Fig. 9) had a very similar overall appearance, comprising both high- and low-affinity components. On the other hand, effects on the slope of the activation curve showed a less complex dependence on Zn^{2+} concentration that could be well described by a single saturation curve (Fig. 10; Eq. 4a). To better delineate the various effects and their differential dependence on Zn^{2+} concentration, Fig. 11 A compares high- and low-affinity K_{Zn} values for shift and slowing and the K_{Zn} value for changes in the slope of the activation curve obtained with 4 mM free Ca^{2+} (pH 7.4). It can be seen that there was no significant difference between the K_{Zn} values for high-affinity shift and slowing, supporting the notion that both effects reflect Zn^{2+} binding to a common site. To obtain a single apparent dissociation constant, we simultaneously refitted the effects on channel voltage dependence and kinetics with a global K_{Zn} value for the high-affinity component (high-affinity 1 in Fig. 11 A) and all other parameters fixed to the values shown in Table S4. The Zn^{2+} concentration for half-maximal shift and slowing thus obtained for recordings performed with 4 mM Ca^{2+} was 4.4 µM, with an 84% CI ranging from 4.2 to 4.6 µM (Fig. 11, A and B; and Table S5). Under the same experimental conditions, the apparent K_{Zn} value was approximately four times higher for effects on the slope of the activation curve (high-affinity 2 in Fig. 11, A and C; and ratio k_{act} in Table S4), >40 times higher for the low-affinity slowing (low-affinity 1 in Fig. 11, A and D; and low-affinity ratio τ_{act} in Table S4), and ~200 times higher for the low-affinity shift in channel voltage dependence (low-affinity 2 in Fig. 11, A and E; and low-affinity $\Delta V_{0.5act}$ and $\Delta V_{0.5inact}$ in Table S4), indicating that there are either multiple Zn^{2+} sites and/or differences in the coupling between Zn^{2+} binding and its various functional consequences.

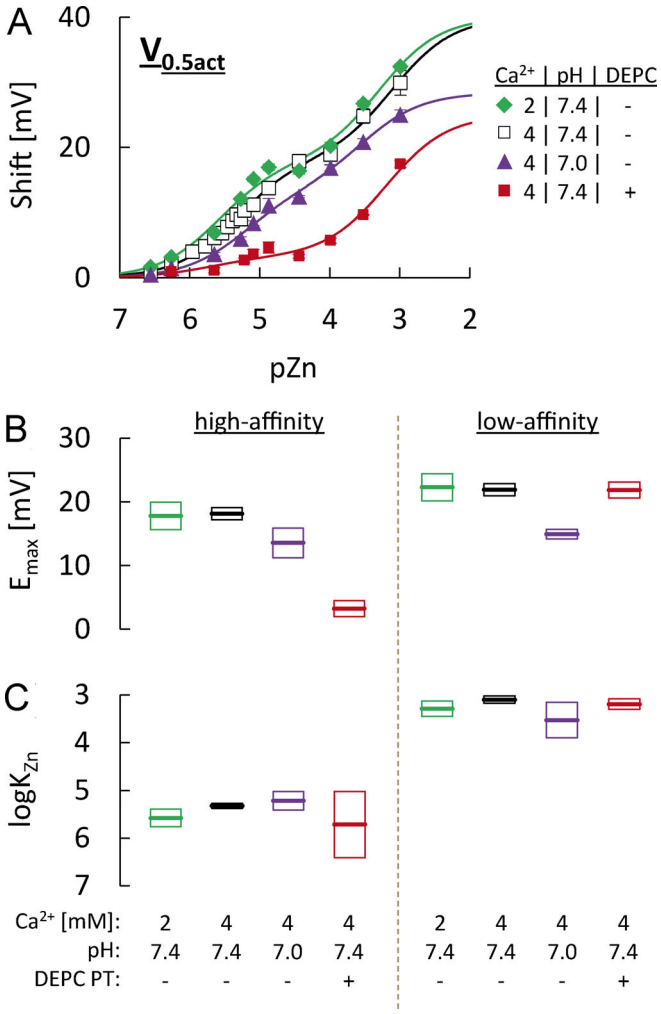

Figure 8. **Concentration dependence for Zn^{2+} effects on activation voltage dependence. (A)** Concentration dependence for the shift in half-activation voltage ($V_{0.5act}$) determined with 4 mM free Ca^{2+} as the charge carrier at pH 7.4 without (open squares, n = 5–12 cells per Zn^{2+} concentration) or with DEPC pretreatment (red squares, n = 5–11 cells per Zn^{2+} concentration), 2 mM free Ca^{2+} as the charge carrier at pH 7.4 (green diamonds, n = 5–8 cells per Zn^{2+} concentration), or 4 mM free Ca^{2+} as the charge carrier at pH 7.0 (purple triangles, n = 5–11 cells per Zn^{2+} concentration). Solid lines are the combination of two binding isotherms for simple bimolecular reactions. **(B and C)** Extrapolated maximum shift (E_{max}; B) and logarithm of apparent dissociation constants ($logK_{Zn}$; C) for the high-affinity (left) and low-affinity (right) components obtained from fits to the data in A. Shown are best-fit values and 84% CIs.

Hallmarks of high-affinity shift and slowing

Pretreatment with DEPC completely eliminated the high-affinity slowing (Fig. 9) and significantly decreased the maximum shift

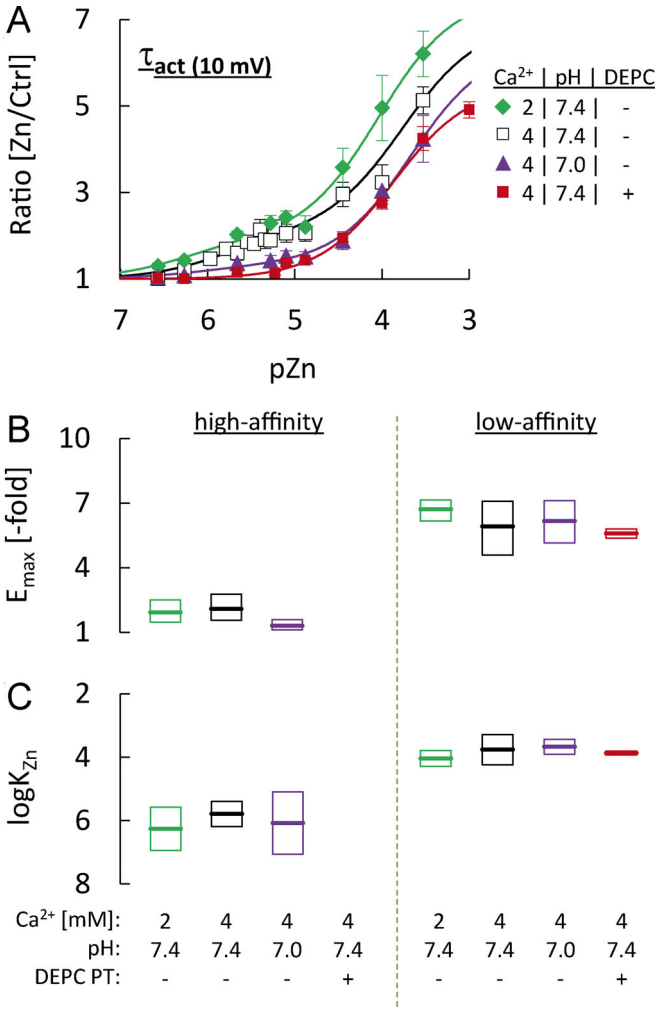

Figure 9. **Concentration dependence for Zn^{2+} effects on activation kinetics. (A)** Concentration dependence for the slowing of activation time constants at 10 mV ($\tau_{act(10mV)}$) determined with 4 mM free Ca^{2+} as the charge carrier at pH 7.4 without (open squares, *n* = 5–12 cells per Zn^{2+} concentration) or with DEPC pretreatment (red squares, *n* = 5–11 cells per Zn^{2+} concentration), 2 mM free Ca^{2+} as the charge carrier at pH 7.4 (green diamonds, *n* = 5–8 cells per Zn^{2+} concentration) or 4 mM free Ca^{2+} as the charge carrier at pH 7.0 (purple triangles, *n* = 5–11 cells per Zn^{2+} concentration). Solid lines are the combination of two binding isotherms for simple bimolecular reactions. **(B and C)** Extrapolated maximum slowing (E_{max}; B) and logarithm of apparent dissociation constants ($logK_{Zn}$; C) for the high-affinity (left) and low-affinity (right) components obtained from fits to the data in A. Shown are best-fit values and 84% CIs.

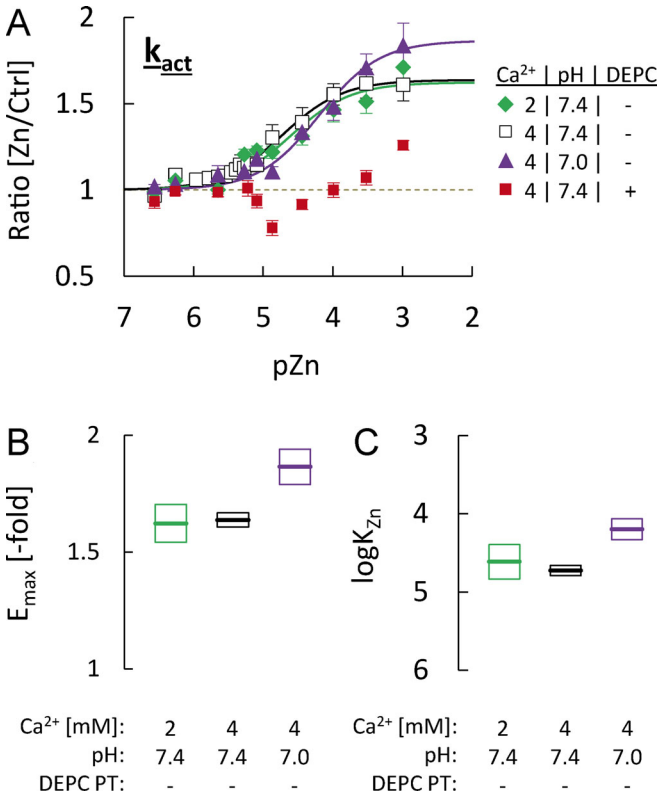

Figure 10. **Concentration dependence for Zn^{2+} effects on activation voltage sensitivity. (A)** Concentration dependence for the increase in activation slope factor (k_{act}) determined under the experimental conditions indicated on the right (same cells as in Fig. 8). Solid lines are binding isotherms for a simple bimolecular reaction. **(B and C)** Extrapolated maximum increase (E_{max}; B) and logarithm of apparent dissociation constants ($logK_{Zn}$; C) obtained from fits to the data in A. Shown are best-fit values and 84% CIs.

mediated by the high-affinity component, which produced, at most, a 3-mV shift (Fig. 8) in pretreated cells. Based on these two findings, DEPC pretreatment antagonized high-affinity Zn^{2+} binding noncompetitively, which is consistent with a disruption of the putative metal binding site by irreversible carbethoxylation of one or more histidine residues.

Reducing the concentration of Ca^{2+} or moderate acidification significantly decreased or increased respectively, the global apparent K_{Zn} value for high-affinity shift and slowing (Fig. 8, Fig. 9, and Fig. 11 B; and Table S5), supporting the notion that there is competition for binding among Zn^{2+}, Ca^{2+}, and protons. In addition, the increase in proton concentration was associated with a significant decrease of the E_{max} values for high-affinity shift and slowing (Fig. 8, Fig. 9, and Fig. 11 B). The latter could only partly be accounted for by the moderate gating effects of pH reduction observed under control conditions (~2-mV shift and 1.2-fold slowing; Table 1), suggesting that protonation of the high-affinity site is either less effective than Zn^{2+}-binding in altering channel gating (i.e., protons could act as weak partial agonists, possibly due to their lower charge) or that protons also reduce Zn^{2+} binding noncompetitively.

On the other hand, reducing the Ca^{2+} concentration had no clear effects on the maximum gating changes mediated by high-affinity binding (Fig. 8, Fig. 9, and Fig. 11 B) or activation gating under control conditions (Table 1), suggesting that Ca^{2+} acts as competitive antagonist that binds to the high-affinity site and displaces Zn^{2+} ions without altering channel gating.

DEPC pretreatment also prevented and partly reversed the direction of changes in k_{act}, but this effect differed from the shift and slowing in that it was completely unaffected by changes in the concentration of Ca^{2+} (Fig. 10 and Fig. 11 C). It was also more sensitive to moderate acidification, which significantly increased the apparent dissociation constant for effects on k_{act} approximately threefold but also significantly increased the E_{max} (Fig. 10, B and C).

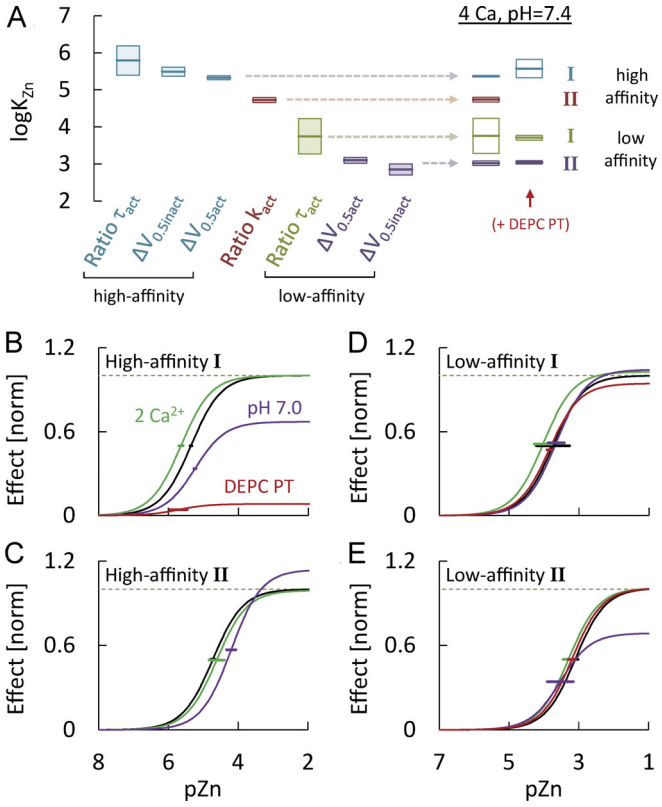

Figure 11. **Concentration dependencies for high- and low-affinity Zn^{2+}-induced gating effects. (A)** Comparison of best-fit logK_{Zn} values and confidence limits for the indicated gating changes obtained in recordings with 4 mM Ca^{2+} at pH 7.4. Note that some of the values shown on the right were obtained by globally fitting the high-affinity shift and slowing (high-affinity I) or the low affinity shift (low-affinity II) with shared K_{Zn} values as described in the text. **(B)** Concentration–response curves, reconstructed from best-fit values obtained by globally fitting the changes in channel voltage dependence ($\Delta V_{0.5act}$, $\Delta V_{0.5inact}$) and kinetics (Ratio τ_{act}) under the indicated conditions with a single, shared K_{Zn} for the high-affinity component and all other values fixed to the values shown in Table S4. For comparison, the extrapolated E_{max} values were normalized by the E_{max} values observed with 4 mM Ca^{2+} at pH 7.4 (black line). **(C–E)** Concentration–response curves reconstructed from best-fit values for the changes in activation slope factor (Ratio k_{act}; C), the low-affinity changes in activation kinetics (Ratio τ_{act}; D), and the low-affinity changes in channel voltage dependence (E). For comparison, the extrapolated E_{max} values were normalized as in B.

Low-affinity shift and slowing have distinct concentration dependencies

Low-affinity shift and slowing were much less affected by DEPC pretreatment (Fig. 8, Fig. 9, and Fig. 11, D and E; and Table S4), suggesting that histidine residues are not involved in these effects. The apparent K_{Zn} value for the shift obtained in recordings performed with 4 mM Ca^{2+} was 790 µM (CI, 660–950 µM), which is significantly higher than the K_{Zn} value for low-affinity slowing of 180 µM (CI, 60–530 µM). For comparison, the corresponding values after pretreatment with DEPC were 640 µM (CI, 500–820 µM) for the low-affinity shift and 140 µM (CI, 120–160 µM) for the low-affinity slowing, respectively (Fig. 11 A). The two effects were also differently affected by moderate acidification, which significantly reduced the K_{Zn} and E_{max} values for low-affinity shift (Fig. 8 and Fig. 11 E), but not slowing (Fig. 9 and Fig. 11 D). Reducing the concentration of Ca^{2+} affected neither the low-affinity shift nor the low-affinity slowing (Fig. 8, Fig. 9, and Fig. 11, D–E). Taken together, these findings are in good agreement with previous studies showing that Zn^{2+} and other d-block metal ions slow activation, often without altering channel voltage dependence, in several VGCCs lacking critical histidine residues in domain I (Magistretti et al., 2001, 2003; Castelli et al., 2003; Park et al., 2015). Interestingly, most of these studies also found a less marked but significant metal-induced slowing of I_{Ca} deactivation speed (Magistretti et al., 2003; Castelli et al., 2003), an effect that was also observed in the present study (Fig. 12). Under normal conditions (i.e., 2 or 4 mM Ca^{2+}, pH 7.4), a clear slowing was only visible at the highest free Zn^{2+} concentrations examined (Fig. 12 B), most likely because the Zn^{2+}-induced depolarizing shift tended to accelerate deactivation at a given test potential, thereby counteracting and masking any potential slowing. Thus, as illustrated in Fig. 12, A and B, the deactivation slowing became much more pronounced and evident already at low micromolar Zn^{2+} levels after DEPC pretreatment and, to some extent, pH reduction, both of which strongly reduced the shift in channel voltage dependence.

Concentration dependence of Zn^{2+}-induced changes in permeation

While the site of action for high-affinity shift and slowing of $Ca_v2.3$ channel currents by Zn^{2+}, Ni^{2+}, and Cu^{2+} is relatively well established, much less is known about the location of additional, lower-affinity sites for d-block metal ions, which appear to be present in most or all high-voltage activated (HVA) Ca^{2+} channels (Neumaier et al., 2015). Since all of these cations can more or less effectively obstruct the ion-conducting pore, and Ca^{2+} channel gating is well known to be influenced by the permeability of charge-carrying ions, it has been proposed that the slowing is independent of the time course and voltage dependence of pore block per se (i.e., not a consequence of time- and voltage-dependent unblock during the test pulses) but related to an allosteric modification of channel gating, induced by binding of metals to their blocking site (Castelli et al., 2003). Block of single HVA Ca^{2+} channels has been shown to occur on a rapid timescale (Winegar et al., 1991), so that II-V current suppression should provide a reasonable measure for the degree of pore block. To assess the apparent voltage dependence of $Ca_v2.3$ channel block by Zn^{2+}, we therefore determined apparent K_{Zn} values for II-V current suppression and plotted them as a function of the test potential (Fig. 13, A and B; but see below). As a simple voltage-independent measure for the degree of "instantaneous" block, we also quantified Zn^{2+} effects on II-V currents in terms of the slope conductance between −40 and +20 mV (G_{II-V}; Fig. 13 C and Table S4). Finally, for comparison with previous work, the degree of "steady-state" block measured with the I-V protocol was quantified based on changes in G_{max} (Table S4).

Although the concentration dependencies exhibited some clear discontinuities at intermediate Zn^{2+} concentrations, they could be reasonably well approximated by a combination of two simple saturation isotherms, the best-fit values of which are

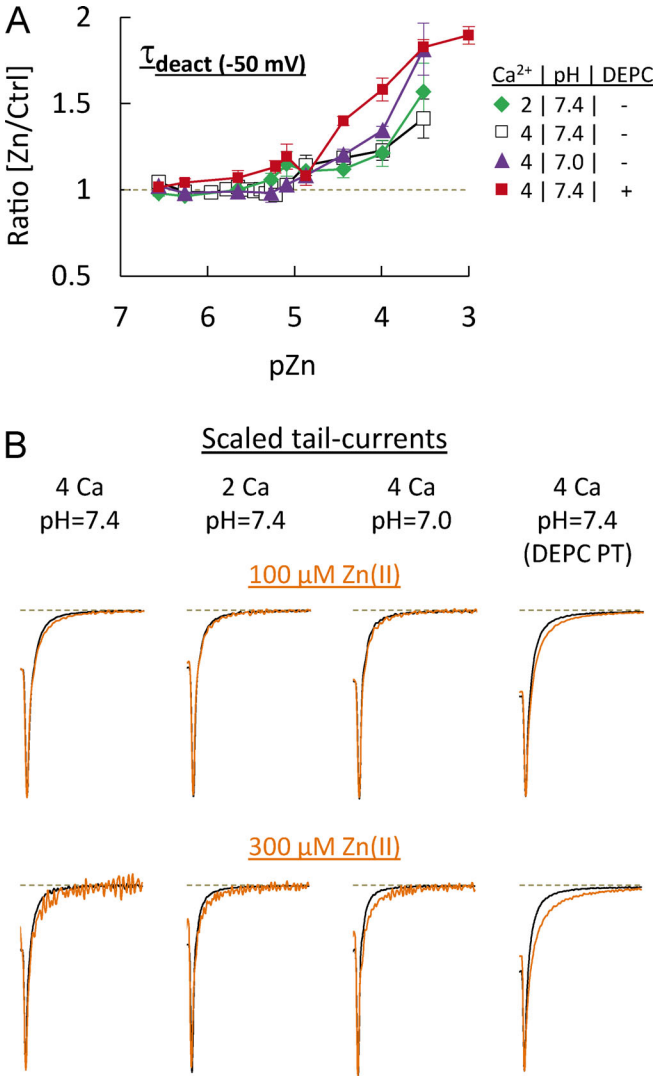

Figure 12. **Concentration dependence for Zn^{2+} effects on tail-current kinetics. (A)** Concentration dependence for the increase in deactivation time-constants at −50 mV ($\tau_{deact(-50\ mV)}$), determined under the experimental conditions indicated on the right (same cells as in Fig. 9). **(B)** Mean tail-current traces recorded under the experimental conditions indicated above in the absence (black) and presence (orange) of 100 µM (top) or 300 µM (bottom) free Zn^{2+}. They have been scaled to their maximum amplitude to highlight kinetic changes.

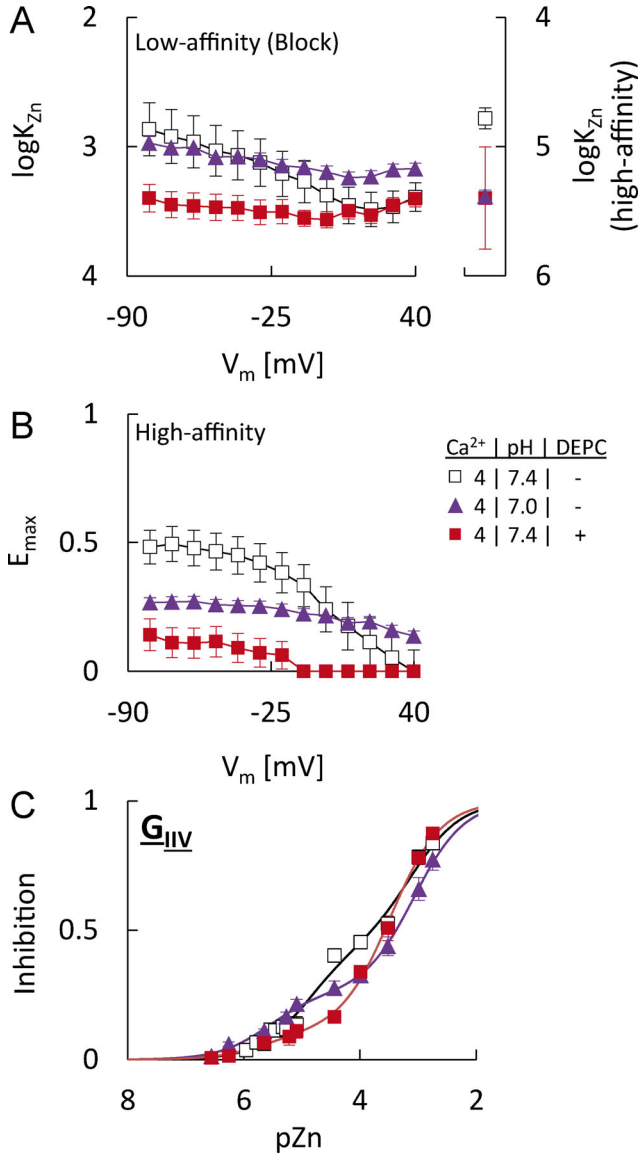

Figure 13. **Voltage and concentration dependence for Zn^{2+} effects on instantaneous (II-V) currents. (A)** Voltage dependence of the logarithm of apparent dissociation constants ($logK_{Zn}$) for low-affinity Zn^{2+}-induced suppression/block of II-V currents under the conditions indicated in B. Also shown in the middle are the voltage-independent $logK_{Zn}$ values for the high-affinity component of II-V current suppression. Note the different scaling of the vertical axis. **(B)** Maximum suppression of II-V currents mediated by the high-affinity component. **(C)** Concentration dependence of II-V current suppression quantified in terms of the slope conductance between −40 and 20 mV (G_{II-V}).

shown in Table S4 and described in more detail in the following sections.

High-affinity binding to histidine residues may also affect conduction

Apparent dissociation constants for high-affinity II-V current suppression showed no clear dependence on the test potential and could be well described with a single, shared K_{Zn} value of 16 µM (CI, 14–20 µM; Fig. 13 A, right), which is in good agreement with the high-affinity K_{Zn} value 12 µm (CI, 9–17 µm; Table S4) obtained when the effects were quantified in terms of changes in G_{II-V}. Suppression mediated by high-affinity binding was incomplete at all test potentials examined (Fig. 13 B), indicating that it is not related to physical obstruction of the ion-conducting pore. In addition, its contribution to total suppression was sensitive to acidification or DEPC pretreatment (Fig. 13 B), suggesting an involvement of histidine residues and possibly other protonation sites. However, while slower activation and faster deactivation due to the Zn^{2+}-induced gating changes may have contributed to a scaling down of instantaneous currents, high-affinity II-V current suppression per se could not be explained by the shift and slowing alone, since it was most prominent at Zn^{2+} concentrations where activation at the prepulse voltage was still complete in under 10 ms (which was the duration of the activating prepulse). In addition, the corresponding K_{Zn} value was significantly higher than the K_{Zn}

for shift and slowing but almost identical to that for the changes in k_{act} (Table S4; see also next section), possibly pointing to a common site of action.

Evidence for a link between pore block and low-affinity changes in gating

K_{Zn} values for low-affinity II-V current suppression were much higher and exhibited a shallow voltage dependence matching the expectations for Ca^{2+} channel block by d-block metal ions (Fig. 13 A). For example, under our standard recording conditions, the logarithm of the K_{Zn} values between −80 and 10 mV could be well described by a straight line $K_{Zn}(V_m) = 443 \times \exp(-0.015 \times V_m)$, indicating that block decreased approximately e-fold per 77 mV with hyperpolarization. In the context of a model where blocking Zn^{2+} ions enter the electric field (compare Woodhull, 1973), the intercept of the line should provide the zero-voltage K_{Zn} value (443 µM; CI, 299–592) and the slope should be equal to $z\delta F/RT$, where z is blocker valence (i.e., +2 for Zn^{2+}) and δ is the fraction of the voltage drop at the blocking site. The value of δ = 0.19 obtained from the above equations corresponds to a blocking site located at ∼20% of the potential drop from the membrane surface, which is in good agreement with previous findings on the voltage dependence of Zn^{2+} block in native HVA Ca^{2+} channels (Winegar et al., 1991). At test potentials more depolarized than 10 mV however, block started to decrease with depolarization, indicating that the voltage dependence is more complex. Moreover, DEPC pretreatment or moderate acidification increased or decreased, respectively, the Zn^{2+} affinity at zero voltage, while both reduced the apparent voltage dependence of block (Fig. 13 A). A more important observation is illustrated in Fig. 14, which compares $\log K_{Zn}$ values for the various Zn^{2+}-induced gating changes (left) with those for block at −50 mV (i.e., the test potential where tail currents for activation curves were determined) or 10 mV (i.e., the test potential where the activation slowing was quantified) and that for high-affinity (voltage-independent) suppression of II-V currents. It can be seen that K_{Zn} values for low-affinity shift and slowing were not significantly different from the K_{Zn} values for block at −50 mV or 10 mV, respectively. Hence, while the low-affinity gating effects could clearly not be accounted for by the shallow voltage dependence of block per se, it seems conceivable that they could be linked to occupation of the blocking site by Zn^{2+}. Also note that, as described in the preceding section, the voltage-independent K_{Zn} value for high-affinity II-V current suppression was almost identical to that obtained for the Zn^{2+}-induced changes in k_{act}.

A Markov model of $Ca_v2.3$ channel gating in the absence of trace metals

To better resolve and separate specific effects of Zn^{2+} on channel gating, we developed a Markov model for $Ca_v2.3$ channels as described below and applied a global fitting procedure, whereby the model was simultaneously fitted to the whole set of recordings obtained under control conditions (4 mM Ca^{2+} at pH 7.4). Because ionic currents alone provide little information on transitions between closed states, the model was further constrained with gating currents (Fig. S2 A), recorded after blocking ion conduction by substitution of Ca^{2+} with Mg^{2+} and addition of 200 µM La^{3+} + 100 µM EDTA (i.e., 100 µM free La^{3+}). The total dataset used for fitting included gating currents recorded at 15 different test potentials, short I-V currents (25 ms) recorded at 15 different test potentials, long I-V currents (400 ms) recorded at 10 different test potentials, II-V currents recorded at 13 different test potentials, and PPI currents recorded at 14 different test potentials.

The topology of the model (Fig. 15 A) was chosen based on the following structural and functional considerations: VGCCs are heterotetrameric proteins composed of four nonidentical VSMs and a central pore region (Fig. 1 A). Optical tracking of voltage-sensor movement by voltage-clamp fluorometry (VCF) in voltage-gated sodium and calcium channels indicates that activation of the individual VSMs is probabilistic in nature and largely governed by their respective steady-state and kinetic properties (Chanda and Bezanilla, 2002; Pantazis et al., 2014). To reflect these findings, horizontal transitions in Fig. 15 A are voltage dependent and correspond to movement of the four nonidentical voltage sensors (rows 1–4 in Fig. 15 B) and pore opening or closing (row 5 in Fig. 15 B), respectively. The voltage sensors operate in parallel and are independent of each other, with one simplifying assumption as described below. The rates for voltage-dependent transitions between two states were expressed in terms of the transition-state theory and are given by

$$k_{fw} = k_{eq} \times exp\left[z \times x \times \left(V_m - V_{eq}\right) \times F/RT\right] \quad (7a)$$

and

$$k_{bw} = k_{eq} \times exp\left[-z \times (1-x) \times \left(V_m - V_{eq}\right) \times F/RT\right], \quad (7b)$$

where k_{fw} and k_{bw} are the values of the forward and backward rates at the test potential V_m, k_{eq} is the value of the forward and backward rates at the test potential V_{eq}, z is the effective valence of the gating charge associated with the transition, x is the relative position of the energy barrier in the membrane, and F, R, and T have their usual thermodynamic meaning (Brog-Graham, 1991).

In voltage-gated sodium channels, activation of the VSMs in domain I-III is associated with rapid charge movement and obligatorily precedes channel opening (Chanda and Bezanilla, 2002), while activation of the VSM in domain I-V is correlated with a slow component of charge movement and gives rise to a short-lived second open state that precedes inactivation (Chen et al., 1996; Capes et al., 2013; Goldschen-Ohm et al., 2013). Much less is known about VGCCs, but mutational studies (Beyl et al., 2016; García et al., 1997) and optical tracking of voltage-sensor movement by VCF (Pantazis et al., 2014; Savalli et al., 2016; Flucher, 2016) indicate that activation of two or three VSMs may be sufficient for pore opening. Consistent with these findings, $Ca_v2.3$ channel gating currents showed a significant fraction of charge movement that was too slow to be associated with channel opening (Fig. S2 B). We tested obligatory models in which activation of 2–4 VSMs is required for channel opening and found that the whole set of ionic and gating current recordings could only be described by a model where activation of two VSMs is obligatory for channel opening, with the simplifying assumption that these VSMs activate in a specific sequence. Based on the role of the VSM that activates first for simulated Zn^{2+}-induced modulation (see next section), we have tentatively assigned these two VSMs the numbers 1 and 2, noting

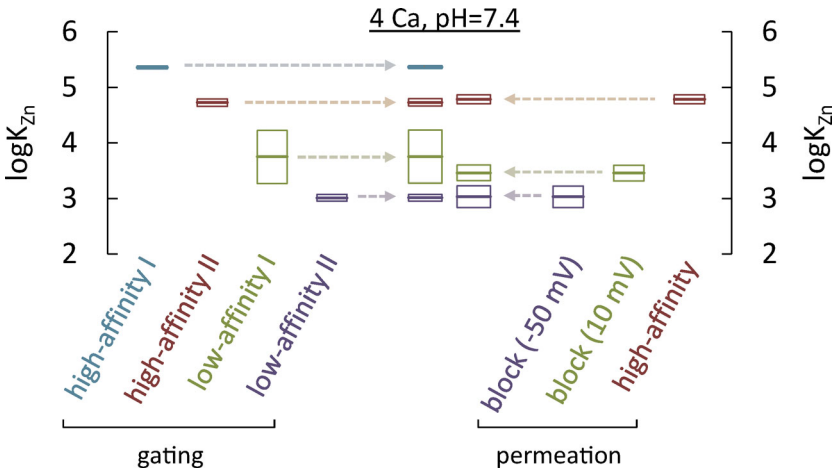

Figure 14. **Concentration dependencies for block and high-affinity suppression of II-V currents.** Comparison of best-fit $logK_{Zn}$ values and 84% confidence limits for the Zn^{2+}-induced high- and low-affinity gating changes (left; for definition, see Fig. 11 A) with the values obtained for the low-affinity component of II-V current suppression/block at −50 mV or 10 mV and the high-affinity voltage-independent component of II-V current suppression (right).

that our data are not sufficient to conclusively relate them to specific protein domains (but see A model of $Ca_v2.3$ channel gating and Zn^{2+}-induced modulation and Limitations). The resulting model has a total of four conductive states, which is consistent with experimental evidence for multiple Ca^{2+} channel open states (Fass and Levitan, 1996; Schneider et al., 1994; Nakayama and Brading, 1993). In analogy to sodium channels, the VSMs not obligatory for channel opening have been proposed to play a role for coupling of activation to voltage-dependent inactivation (Pantazis et al., 2014; Flucher, 2016), a process that has been shown or is thought to be state rather than truly voltage dependent in VGCCs (Neumaier et al., 2015). Therefore, vertical transitions in the model are voltage independent and correspond to entry into and return from fast (Fig. 15 A, middle) and slow (Fig. 15 A, bottom) inactivated states. As the VSMs in the model could not be related to specific domains of the channel protein and data on the coupling between voltage-sensor movement and voltage-dependent inactivation is not available, the

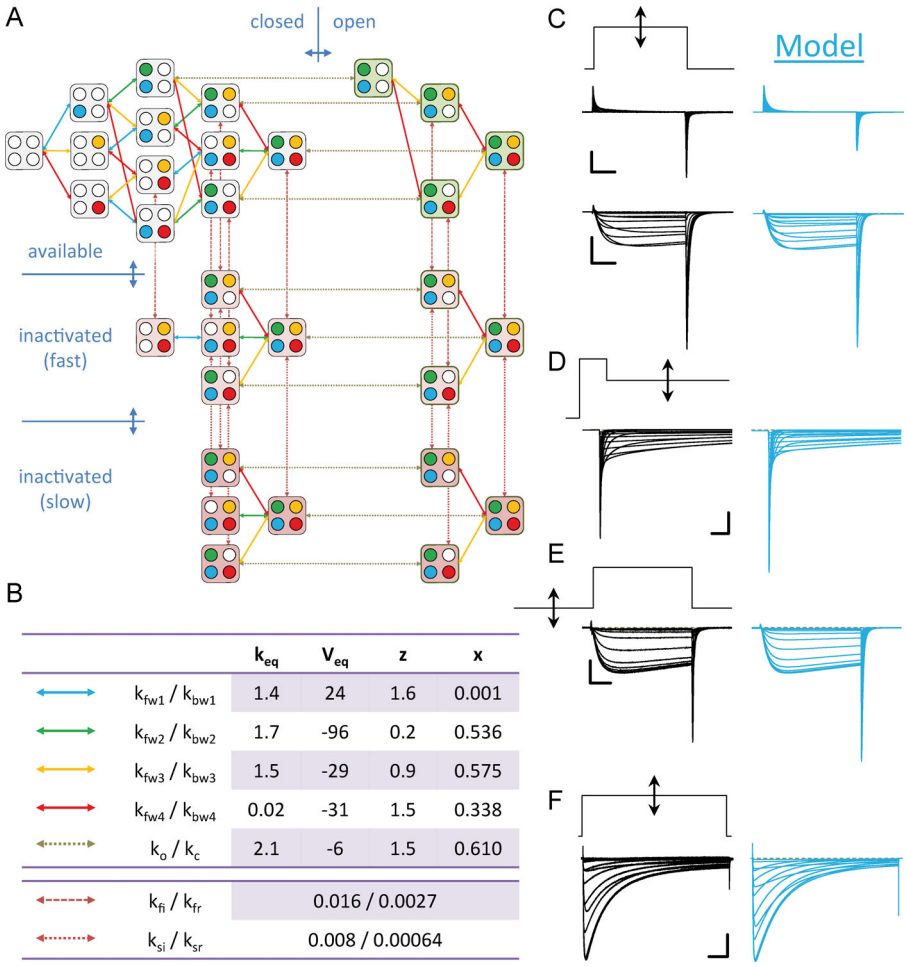

	k_{eq}	V_{eq}	z	x
k_{fw1} / k_{bw1}	1.4	24	1.6	0.001
k_{fw2} / k_{bw2}	1.7	-96	0.2	0.536
k_{fw3} / k_{bw3}	1.5	-29	0.9	0.575
k_{fw4} / k_{bw4}	0.02	-31	1.5	0.338
k_o / k_c	2.1	-6	1.5	0.610
k_{fi} / k_{fr}	0.016 / 0.0027			
k_{si} / k_{sr}	0.008 / 0.00064			

Figure 15. **A Markov model of $Ca_v2.3$ channel gating. (A)** Topology of a Markov model that accounts for most salient features of $Ca_v2.3$ channel gating under control conditions. Horizontal transitions are voltage dependent and correspond to movement of four nonidentical voltage sensors and channel opening or closing, with rate constants expressed in terms of the transition state theory (for details, see text). Vertical transitions are voltage independent and correspond to entry into and return from fast (middle) and slow (bottom) inactivated states. Transitions between inactivated states are identical to the parallel transitions between closed and open states. **(B)** Overview of individual transitions of the model and optimized parameter values obtained by globally fitting the model to the whole set of control recordings obtained with 4 mM Ca^{2+} at pH 7.4. **(C–F)** Comparison of recorded (black) and simulated (turquoise) families of current traces evoked with the protocols depicted above. Source code for the model is available in ModelDB (McDougal et al., 2017) at http://modeldb.yale.edu/261714.

state dependence of inactivation was determined empirically by fixing fast and slow inactivation and deinactivation time constants to experimentally determined values and adding or removing inactivated states until the model reproduced both the time-course and steady-state voltage dependence of inactivation. Microscopic reversibility was imposed by defining transition rates between inactivated states as being identical to those of the (parallel) transitions between closed states.

The individual transitions of the model and optimized parameter values obtained from fits to the control recordings are listed in Fig. 15 B. Fig. 15, C–F compare recorded families of current traces evoked with the voltage protocols depicted above (black) and simulations (blue) performed with the optimized parameter values. For further comparison, the simulated currents were analyzed in the same way as the experimental data, and the results are plotted together in Fig. S3. The model accounted for all salient features of the control data, including the time course of macroscopic current activation, deactivation, and inactivation (Fig. 15, C–F); the shape and position of the I-V curve (Fig. S3 A); the relatively sharp separation between voltage-dependent activation and inactivation (Fig. S3 B); the bell-shaped voltage dependence of activation and deactivation time constants (Fig. S3 D); and the fast and slow gating current components (Fig. 15 C, top).

Modeling the effects of Zn^{2+} on $Ca_v2.3$ channel gating

Lacking data from, for example, VCF, the voltage sensors in our model could obviously not be related to specific domains in the channel protein. However, preliminary tests with the model showed that only manipulation of one set of voltage-dependent transitions (i.e., k_{fw1}/k_{bw1} in Fig. 15 B) could qualitatively reproduce the selective slowing of activation gating observed experimentally, while changes in the other transition had either little effect on activation kinetics (k_{fw3}/k_{bw3} and k_{fw4}/k_{bw4}) or affected the deactivation kinetics in a way that was inconsistent with the experimental data (k_{fw2}/k_{bw2} and k_o/k_c). With this is mind, we first extended our model by including Zn^{2+} binding to a first site (site 1) with a resulting modification of voltage sensor 1 in the model to simulate the Zn^{2+}-induced high-affinity changes in activation gating.

To this end, each state in the model was connected to a corresponding Zn-bound state, with rates for binding (k_{on1}) and unbinding (k_{off1}) at site 1 defined in terms of a simple, bimolecular reaction (Eq. 5a and Eq. 5b). To simulate Zn^{2+}-induced changes in gating rates, we adopted the shift and scaling procedure first introduced by Elinder and Arhem (2003) and assumed that the rate constants for movement of voltage sensor 1 in metal-bound channels can be expressed by modification of Eq. 7a and Eq. 7b into

$$k_{fw1} = A_{off1} \times k_{eq} \times exp\left[z_1 \times x_1 \times \left(V_m - V_{eq1} - V_{off1}\right) \times F/RT\right] \quad (8a)$$

and

$$k_{bw1} = A_{off1} \times k_{eq} \times exp\left[-z_1 \times (1 - x_1) \times \left(V_m - V_{eq1} - V_{off1}\right) \times F/RT\right], \quad (8b)$$

where V_{off1} is a voltage offset that accounts for the electrostatic effects of a bound metal ion on the local electric field at sensor 1 and A_{off} is a slowing factor that accounts for the mechanical effects of a bound metal ion on sensor 1 and corresponds to adding an energy barrier of $\Delta W = kT \times \ln(A_{off}^{-1})$.

Table 2. **Parameters used for simulation of Zn^{2+} effects in Figs. 16, 17, 18, and 19**

Parameter	Site 1	Site 2
K_{Zn1} [mM^{-1}]	0.003	0.1
d_{Zn} [$mM^{-1}ms^{-1}$]	100	100
A_{off}	0.05	0.3
V_{off} [mV]	50	-

Pore block and the low-affinity slowing of activation and deactivation were implemented by including a second, lower-affinity Zn^{2+} blocking site, with rates for binding (k_{on2}) and unbinding (k_{off2}) defined as above (Eq. 5a and Eq. 5b). Channels with Zn^{2+} bound to site 2 were assumed to be nonconductive (i.e., blocked) and their rates for opening and closing slowed by an unidentified allosteric mechanism implemented as slowing factor A_{off2}. For simplicity, block was assumed to be voltage independent and restricted to activated closed and open channel states.

Fig. 16, Fig. 17, and Fig. 18 show results from simulations for a Zn^{2+} concentration of 5.4 µM performed with the extended model and parameter values shown in Table 2. It can be seen that, despite the many simplifying assumptions, the model reproduced almost exactly the corresponding experimental data, with much stronger suppression of I-V versus II-V currents (Fig. 16, A and C–E), a depolarizing shift of the activation voltage dependence (Fig. 16 F), a dramatic slowing of macroscopic activation with little change in deactivation time constants (Fig. 17, A and B; and Fig. 18 A), and an apparent acceleration of tail-current decay measured with the II-V protocol at depolarized test potentials (Figs. 17 B and 18 C). In addition, simulated Zn^{2+}-modified currents showed the same apparent slowing of inactivation kinetics near the half-activation voltage as observed experimentally (Fig. 17 A; and Fig. 18, B and D) and a similar shift of the inactivation voltage dependence (Fig. 16 F), supporting the assumption that these effects could result from activation–inactivation coupling rather than Zn^{2+}-induced changes in the microscopic inactivation rates. The model underestimated the magnitude of II-V current suppression at low Zn^{2+} concentrations and overestimated it at high Zn^{2+} concentrations, which is not surprising given that we have neglected the voltage dependence of block and the high-affinity component of II-V current suppression. However, the predicted concentration dependence of I-V current suppression, quantified in terms of the G_{max}, was in good agreement with the experimental data (Fig. 16 G). Even more importantly, the model qualitatively and quantitatively reproduced the concentration dependence of Zn^{2+} effects on activation voltage dependence (Fig. 19 A), macroscopic activation (Fig. 19 B), and deactivation kinetics (Fig. 19 D) in the range of physiologically relevant Zn^{2+} concentrations. Interestingly, the model also reproduced the small but significant and Zn^{2+}-concentration–dependent increase in apparent V_{rev} (Fig. 19 C), indicating that this effect was not related to true changes in,

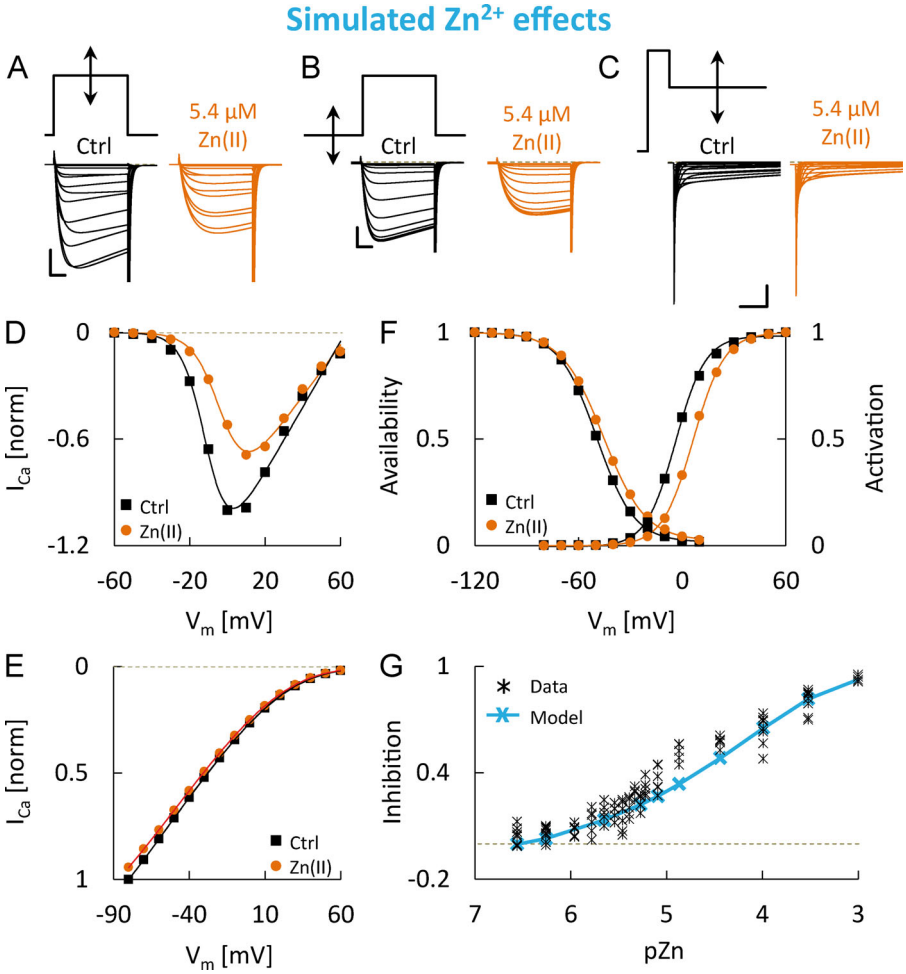

Figure 16. **Simulated Zn^{2+} effects on $Ca_v2.3$ channel voltage dependence. (A–C)** Families of simulated current traces evoked with the protocols depicted above (for details, see Fig. 2), with the free Zn^{2+} concentration set to 0 (black) or 5.4 µM (orange). Scale bar corresponds to 5 ms and 20 pA/pF in A, 5 ms and 50 pA/pF in B, or 10 ms and 200 pA/pF in C. **(D)** I-V relationships determined from the simulated currents shown in A. **(E)** II-V relationships determined from the simulated currents shown in C. **(F)** Isochronous activation (right) and PPI (left) curves determined from the simulated tail currents in A or the simulated peak currents in B, respectively. **(G)** Concentration dependence of simulated Zn^{2+}-induced suppression, quantified in terms of changes in G_{max} of simulated currents observed when the free Zn^{2+} concentration was increased from 0 to 1,000 µM.

for example, equilibrium potentials or selectivity and highlighting the ineptness of V_{rev} as a measure for true V_{rev} values under conditions that alter channel voltage dependence. It also qualitatively reproduced the concentration dependence of changes in inactivation voltage dependence, although it did underestimate the degree of shift (Fig. 19 E), which could reflect the arbitrary state dependence of inactivation and/or the disregard of ultraslow inactivation processes. On the other hand, the model did clearly not account for the reduced steepness of the activation curve (Fig. 19 F), even though it did predict a minor increase of k_{act} at the highest free Zn^{2+} concentration. Taken together, this is consistent with our findings that the mechanism underlying the changes in k_{act} is somewhat different from that involved in the shift and slowing.

Discussion

Endogenous, loosely bound Zn^{2+} ions are increasingly recognized as potential modulators of neuronal excitability, and Zn^{2+} dis-homeostasis has been implicated in a number of pathophysiological conditions (Frederickson et al., 2000, 2005; Mathie et al., 2006). Owing to a high-affinity trace metal–binding site in their domain I VSM (Fig. 1 A), which is not conserved in other HVA VGCCs, $Ca_v2.3$ channels are among the most sensitive targets for Zn^{2+} and certain other trace metals currently known (Kang et al., 2007; Shcheglovitov et al., 2012). Here, we performed an in-depth assessment of Zn^{2+}-induced modulation of cloned human $Ca_v2.3 + \beta_3$ channels over a wide range of Zn^{2+} concentrations and used a preliminary Markov model to test whether the results can be accounted for by different biophysical mechanisms. Our most important and novel findings are (1) that low micromolar Zn^{2+} concentrations could both inhibit or stimulate Ca^{2+} influx through $Ca_v2.3$ channels depending on RMP (Figs. 5 and 6); (2) that multiple high- and low-affinity mechanisms of Zn^{2+} action exist, which can be distinguished based on their concentration dependence, sensitivity to the experimental conditions, and correlation with pore block (Figs. 7, 8, 9, 10, 11, 12, 13, and 14); and (3) that most, but not all, of the observed effects can be described by a simplified model that involves Zn^{2+} binding to a first site with an associated electrostatic modification and mechanical slowing of one of the voltage sensors and Zn^{2+} binding to a second, lower-affinity site, which blocks the channel and modifies the opening and closing transitions (Figs. 16, 17, 18, and 19). In the following sections, we will try to reconcile our findings with previous results and discuss potential implications with regard to the underlying sites, briefly consider our proposed model and potential (patho)physiological implications, and finally address some inherent limitations of our work.

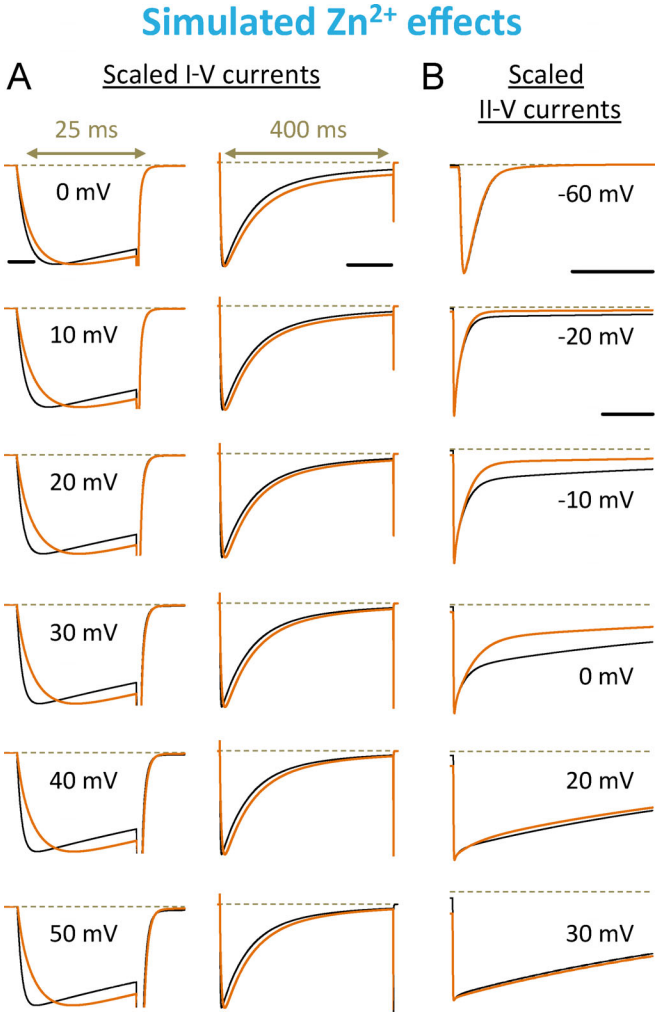

Figure 17. **Simulated Zn^{2+} effects on the shape of macroscopic Ca^{2+} currents. (A)** Simulated I-V current traces evoked in response to 25 ms (left) or 400 ms (right) voltage steps to the indicated test potentials, with the free Zn^{2+} concentration set to 0 (black) or 5.4 µM (orange). They have been scaled to their maximum amplitude to highlight kinetic changes. Scale bars correspond to 10 and 100 ms for short and long voltage steps, respectively. **(B)** Simulated II-V current traces evoked at the indicated test potentials, with the free Zn^{2+} concentration set to 0 (black) or 5.4 µM (orange). They have been scaled to their maximum amplitude to highlight kinetic changes. Scale bars correspond to 2 ms for the tail current at −60 mV and 10 ms for all other test potentials.

Evidence for multiple mechanisms of Zn^{2+} action

Various previous studies have investigated the effects of Zn^{2+} and other trace metals on native or cloned VGCCs, all of which are thought to be more or less potently blocked by these cations. With regard to cloned $Ca_v2.3$ channels, (sub)micromolar concentrations of Zn^{2+}, Cu^{2+}, and Ni^{2+} have also been shown to produce depolarizing shifts in channel voltage dependence, a reduced sensitivity toward depolarization, and a pronounced slowing of macroscopic activation (Zamponi et al., 1996; Shcheglovitov et al., 2012; Kang et al., 2007), resembling their action on native R-type currents in cortical (Castelli et al., 2003; Magistretti et al., 2003) and dorsal root ganglion neurons (Shcheglovitov et al., 2012). Our present findings reveal that the Zn^{2+}-induced gating changes can be separated into multiple components with distinct concentration dependencies, which comprise a common high-affinity component for shift and slowing (K_{Zn} ~2–3 µM with 2 mM Ca^{2+}), a second high-affinity component for the changes in activation voltage sensitivity (K_{Zn} ~15–40 µM with 2 mM Ca^{2+}), and two lower-affinity components for shift (K_{Zn} >500 µM with 2 mM Ca^{2+}) and slowing (K_{Zn} ~50–170 µM with 2 mM Ca^{2+}).

High-affinity shift and slowing

To delineate effects mediated by Zn^{2+} binding to histidine residues, we used DEPC pretreatment, which effectively prevented the high-affinity shift and slowing. This is consistent with molecular cloning studies showing that the effects of Zn^{2+}, Cu^{2+}, and Ni^{2+} are all diminished by mutation of histidine residues located in the IS1-IS2 (His^{111}) and IS3-IS4 (His^{179} and His^{183}) loops (Fig. 1 A; Kang et al., 2007; Shcheglovitov et al., 2012). In particular, substitution of two loop histidines has previously been shown to reduce the activation shift induced by 7 µM Zn^{2+} from 13 mV in WT channels to 3 mV in mutant channels (with 1 mM Ca^{2+}; Shcheglovitov et al., 2012). Considering that interpolation of our own data to the same free Zn^{2+} concentration gives a shift of 11 or 13 mV (with 4 or 2 mM Ca^{2+}) for untreated and 3 mV (with 4 mM Ca^{2+}) for DEPC-treated channels, it seems justified to conclude that high-affinity shift and slowing reflect Zn^{2+} interaction with the proposed metal binding site and that DEPC mainly acted by modification of histidine residues in the same site (but see Limitations). Moderate acidification significantly reduced apparent Zn^{2+} affinity and maximum Zn^{2+} effects and produced gating changes similar to Zn^{2+} under control conditions, which is consistent with previous results showing that metal ions and protons both alter $Ca_v2.3$ channel gating by interaction with the known loop histidines (Cens et al., 2011; Shcheglovitov et al., 2012). In view of our findings, protons could act as partial agonists that are less effective than Zn^{2+} in altering channel gating, whereas the effects of Ca^{2+} on apparent Zn^{2+} affinity are consistent with a competitive antagonism.

Unexpectedly, low micromolar Zn^{2+} concentrations also stimulated $Ca_v2.3$ channel currents evoked from moderately depolarized holding potentials, which may have important (patho)physiological implications (see (Patho)physiological implications). Development and reversal of this effect were much slower than Zn^{2+}-induced suppression but could be reproduced by a change in holding potential approximately equal to the shift in channel voltage dependence, suggesting that they reflect equilibration of a slow coupled inactivation process rather than slow Zn^{2+} binding/unbinding at a distinct, stimulatory site.

High-affinity changes in slope factor

Another unexpected finding was that the K_{Zn} for high-affinity shift and slowing (4.2–4.6 µM) is roughly four times smaller than the K_{Zn} for changes in voltage sensitivity (16–22 µM), even though both effects were sensitive to histidine modification. In principle, this could reflect the fact that Zn^{2+} preferentially affects the charge movement of only one of the four pseudosubunits. However, we also found that (1) DEPC produces effects opposite to the Zn^{2+}-induced shift and slowing but mimics Zn^{2+} effects on the activation slope factor under control conditions,

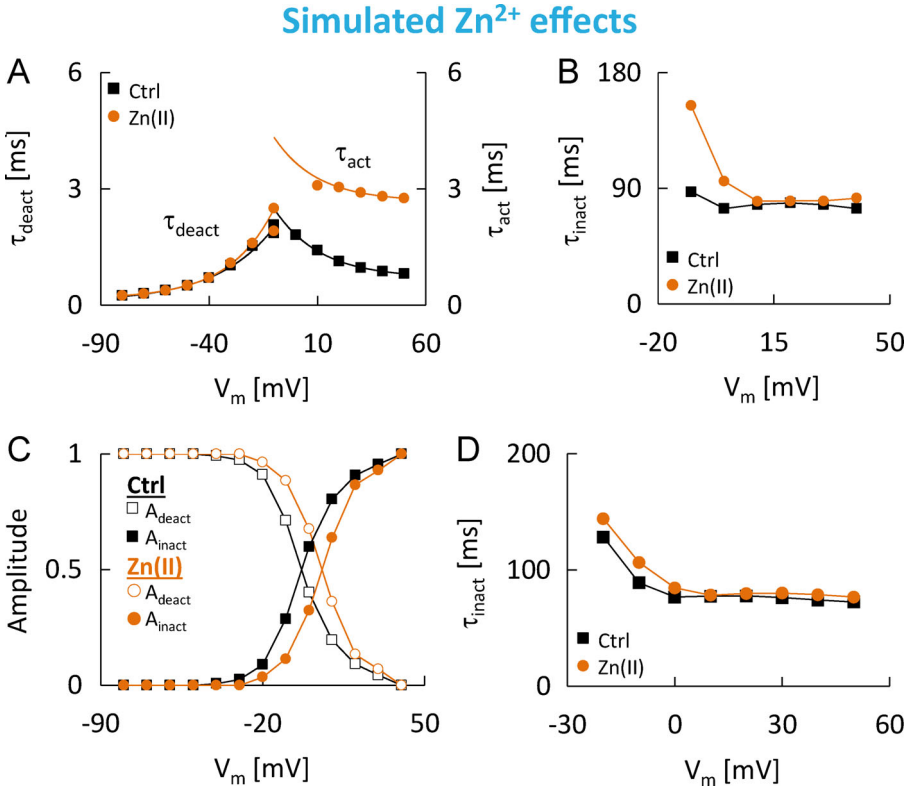

Figure 18. **Simulated Zn^{2+} effects on macroscopic activation, deactivation, and inactivation kinetics. (A)** Activation (right) and deactivation (left) time constants, determined by exponential fits to the rising phase of simulated I-V currents or the decaying phase of simulated II-V currents, with the free Zn^{2+} concentration set to 0 (black squares) or 5.4 µM (orange circles). **(B)** Inactivation time constants determined from exponential fits to the decay of simulated II-V currents at depolarized test potentials, with the free Zn^{2+} concentration set to 0 (black squares) or 5.4 µM (orange circles). **(C)** Contribution of deactivation (open symbols) and inactivation (filled symbols) to total decay of simulated II-V currents, with the free Zn^{2+} concentration set to 0 (black squares) or 5.4 µM (orange circles). **(D)** Inactivation time constants, determined by fitting a single exponential function with variable offset to the decaying phase of simulated currents evoked by 400-ms voltage steps to the indicated test potentials, with the free Zn^{2+} concentration set to 0 (open squares) or 5.4 µM (orange circles).

(2) shift and slowing show a different dependence on the experimental conditions than the changes in the slope of the activation curve, and (3) the proposed model quantitatively accounts for the shift and slowing, but not for the increase in slope factor. In addition, the K_{Zn} for changes in slope factor coincided almost exactly with the K_{Zn} for a voltage-independent decrease of II-V currents (14–20 µM) that was also sensitive to DEPC pretreatment. The underlying mechanism remains to be firmly established, but it is tempting to speculate that Zn^{2+} mimics the proton-induced decrease in $Ca_v2.3$ channel unitary conductance described in a previous study, which has been linked to a histidine residue in one of the pore loops (Fig. 1 A) and is also accompanied by an increased slope factor (Cens et al., 2011). However, DEPC sensitivity alone does not necessarily prove a role of histidine residues, and the fact that acidification actually increased the maximum changes in slope factor could point to the involvement of other amino acid residues (see Limitations). In any case, the moderate magnitude of the slope changes even at saturating Zn^{2+} concentrations (~1.7-fold increase in k_{act}) suggests that reduced voltage sensitivity does not significantly contribute to the net Zn^{2+} action, which is also supported by our modeling results.

Low-affinity slowing

Our findings also indicate that an unidentified, DEPC-resistant site with lower Zn^{2+} affinity contributes to the slowing observed at higher free Zn^{2+} levels and that the same site could be involved in Zn^{2+}-induced block measured with the II-V protocol. K_{Zn} values for the low-affinity slowing were ~150 µM and well separated from those for the low-affinity shift. Interestingly, Zn^{2+} and other trace metal ions have been shown to slow activation of several native HVA Ca^{2+} channels lacking critical histidine residues in domain I (Magistretti et al., 2001, 2003; Castelli et al., 2003), so that the site involved in the slowing could be shared with other members of the family. Because Ca^{2+} channel block and permeation are thought to be governed by the same principles, and Ca^{2+} channel gating is well known to be affected by the nature of permeating ions (for review, see Neumaier et al., 2015), the metal-induced slowing has been proposed to reflect an allosteric effect linked to occupation of the pore (Castelli et al., 2003), an idea that is reinforced by our electrophysiological and modeling results (see A model of $Ca_v2.3$ channel gating and Zn^{2+}-induced modulation). Based on the shallow voltage dependence of low-affinity II-V current suppression, the putative Zn^{2+}-blocking site in $Ca_v2.3$ channels could reside in or at a superficial part of the pore near the outer vestibule rather than deep within the electric field, which is consistent with a number of previous studies on VGCC block by d-block metal ions (Winegar et al., 1991; Díaz et al., 2005; Lopin et al., 2012). As such, one promising candidate site appears to be a putative EF-hand motif located external to the selectivity filter EEEE-locus and outside of the narrow pore region (Fig. 1 A), which is present in all HVA Ca^{2+} channels and has previously been implicated in their differential sensitivity to Zn^{2+} block (Sun et al., 2007). Lack of this site in low-voltage activated channels could explain why the effects of Zn^{2+} on these channels appear to be much less uniform, with several studies in different preparations reporting inconsistent or even contradictory findings (Cataldi et al., 2007; Traboulsie et al., 2007; Sun et al., 2007; Noh et al., 2010).

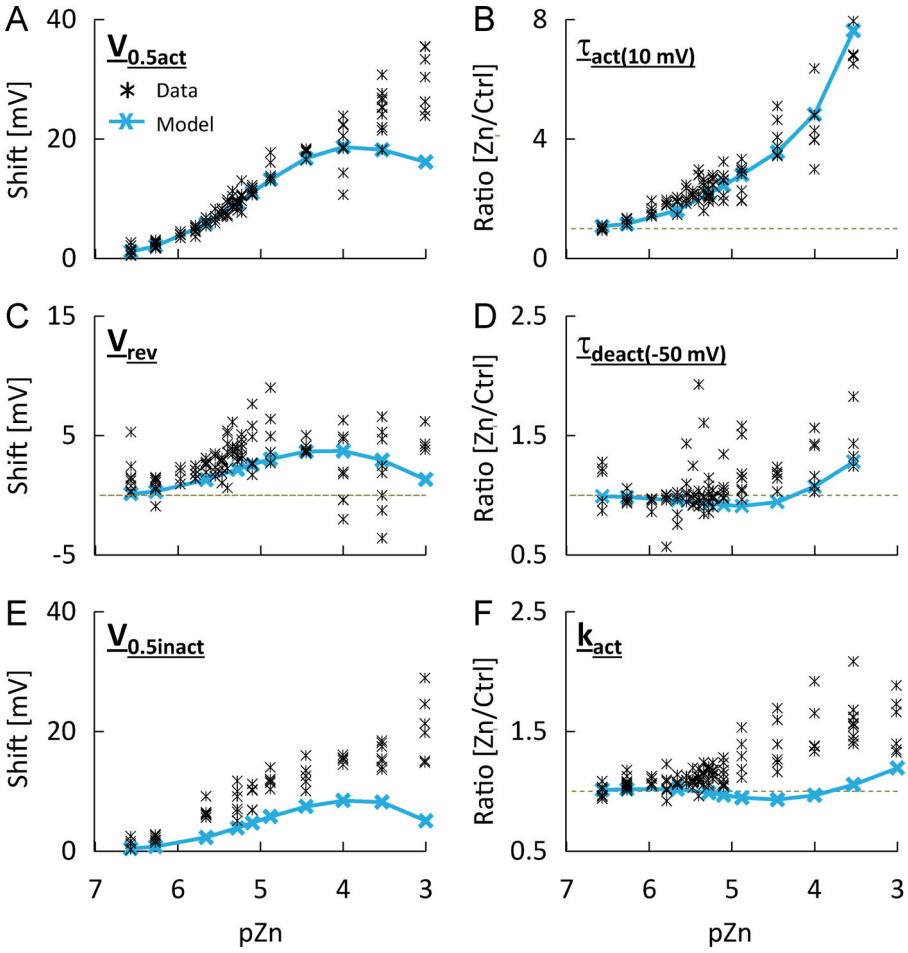

Figure 19. **Concentration dependence of simulated Zn^{2+} effects on $Ca_v2.3$ channels. (A–F)** Comparison of measured and simulated concentration dependencies for Zn^{2+}-induced changes in half-activation voltage (A), activation time constant at 10 mV (B), apparent V_{rev} (C), deactivation time constant at −50 mV (D), half-inactivation voltage (E), and activation slope factor (F).

Low-affinity shift

K_{Zn} values for the low-affinity shift were >500 µM and similar for activation and inactivation voltage dependence. The concentration dependence suggested that this effect might also be related to block measured with the II-V protocol, but because it is unlikely to ever become significant under (patho)physiological conditions, we have neglected it in our modeling study.

A model of $Ca_v2.3$ channel gating and Zn^{2+}-induced modulation

Gating models provide quantitative predictions that can be used to test hypotheses about molecular mechanisms and understand the role of voltage-gated ion channels in electrical excitability and cell signaling. Here, we developed a preliminary Markov model for $Ca_v2.3$ channel voltage-dependent gating that is consistent with the available data on channel structure and accurately reproduces most salient features of ionic and gating currents under near-physiological ionic conditions. Voltage-sensor activation in the model is probabilistic in nature and only governed by the respective steady-state and kinetic properties, with the simplifying assumption that two of the VSMs activate in a specific sequence. The latter is at odds with a VCF study on $Ca_v1.2$ channels, where fluorescent changes in all four domains occurred without a discernible lag (Pantazis et al., 2014), but it has been shown that sequential and parallel activation models may not always be resolvable from each other in electrophysiological recordings (Chanda and Bezanilla, 2002). The model also incorporates recent findings that activation of only two VSMs may be obligatory for Ca^{2+} channel opening (Pantazis et al., 2014), an idea that is reinforced by (1) a slow component of charge movement observed in our own and previous Ca^{2+} channel gating current recordings (Josephson and Varadi, 1996; Josephson, 1997), (2) evidence for multiple Ca^{2+} channel open states (Fass and Levitan, 1996; Schneider et al., 1994; Nakayama and Brading, 1993), and (3) the success of HH m^2h-type models in describing Ca^{2+} channel ionic currents (Sala, 1991; Kostyuk et al., 1977; Kay and Wong, 1987; Benison et al., 2001).

In addition, our model provides insight into potential mechanisms of Zn^{2+}-induced modulation and shows that electrostatic modification and mechanical slowing of a single VSM mediated by Zn^{2+} binding to a common site could quantitatively account for the high-affinity shift and slowing and also explain the observed changes in macroscopic inactivation if the process is state dependent and coupled to activation.

The low-affinity slowing was modeled as an allosteric effect that results from occupation by Zn^{2+} of a pore blocking site, which could well account for the experimental data, even though we made several simplifying assumptions. As such, the modeling results also confirm that slower opening of blocked channels could result in slower macroscopic currents even though only nonblocked channels contribute to these currents,

which might account for the fact that many inorganic blockers also alter Ca^{2+} channel gating (Neumaier et al., 2015). Given that we have only circumstantial evidence for an intrapore location of the site involved in low-affinity slowing, other models could almost certainly account for these findings as well, albeit at the cost of more complicated model structures with additional binding sites. In addition, until exact VCF data on $Ca_v2.3$ channel voltage-sensor movement become available, structural interpretation of the model in terms of specific protein domains remains problematic (see also Limitations). Regardless of its physical interpretation, however, our model faithfully reproduces $Ca_v2.3$ channel gating in the absence of trace metals and most hallmarks of Zn^{2+}-induced suppression as well as their dependence on Zn^{2+} concentration. It is freely available at ModelDB (accession number 261714) and can be readily integrated into existing cell models, making it a useful tool for future studies on the physiological role of $Ca_v2.3$ channels and/or the effects of synaptic Zn^{2+} release on electrical excitability and cell signaling.

(Patho)physiological implications

Although some have questioned that synaptic Zn^{2+} can exceed 1 µM (Erreger and Traynelis, 2005; Vergnano et al., 2014), most studies suggest that physiological peak cleft concentrations at Zn^{2+} enriched synapses could reach at least low micromolar levels, especially during intense, LTP-inducing stimulation (Aniksztejn et al., 1987; Assaf and Chung, 1984; Besser et al., 2009; Howell et al., 1984; Kodirov et al., 2006; Qian and Noebels, 2005, 2006; Vogt et al., 2000; Ueno et al., 2002; Komatsu et al., 2005; Li et al., 2001; Quinta-Ferreira et al., 2016). One of our most important findings may therefore be that low micromolar Zn^{2+} concentrations could inhibit or stimulate Ca^{2+} influx through $Ca_v2.3$ channels depending on RMP. In addition, slow reversal of the stimulation during washout at depolarized RMP could result in a paradoxical increase of Ca^{2+} influx above the control level that persists for some time after cessation of the Zn^{2+} signal. The latter is especially interesting, because rises in synaptic Zn^{2+} concentrations during neuronal activity have been shown or are thought to be transient in nature (Vergnano et al., 2014; Quinta-Ferreira et al., 2016). As such, it could potentially provide a link between Zn^{2+} signals and certain plasticity processes like presynaptic LTP at hippocampal mossy fiber synapses, which is in part mediated by $Ca_v2.3$ channels (Dietrich et al., 2003) and has been shown to depend on synaptic Zn^{2+} release in brain slice recordings (Pan et al., 2011). In principle, the holding potential dependence of Zn^{2+} effects could also be involved in the reported proictogenic role of $Ca_v2.3$ channels (Weiergräber et al., 2006a, 2007; Dibué-Adjei et al., 2017), since depolarization of the neuronal RMP due to, for example, spreading depolarization or paroxysmal depolarizing shifts might lead to a decrease in the inhibitory action or even reverse the direction of Zn^{2+} effects. Considering that even very small changes in ion channel function (Thomas et al., 2009) and synaptic gain (Du et al., 2019) can lead to seizure-like activity, reduced $Ca_v2.3$ channel suppression by Zn^{2+} could conceivably contribute to the ictogenic processes when the brain moves into a proseizure state.

Because maximum Zn^{2+} cleft concentrations have not been established with sufficient certainty, the potential relevance of low-affinity Zn^{2+}-induced modulation in the brain remains ambiguous. However, the slowing effect could be important in certain tissues outside of the brain, such as in pancreatic islets of Langerhans, where local Zn^{2+} concentrations during cosecretion of Zn^{2+} and insulin have been estimated to reach several hundred micromoles (Kim et al., 2000). Animal studies have linked $Ca_v2.3$ channels to α-cell glucagon (Pereverzev et al., 2005), β-cell insulin (Jing et al., 2005; Matsuda et al., 2001; Pereverzev et al., 2002), and δ-cell somatostatin (Zhang et al., 2007) secretion and we have previously shown that they are involved in intra-islet paracrine Zn^{2+} signaling (Drobinskaya et al., 2015). However, further studies will clearly be required to firmly establish whether the low-affinity effects described here are physiologically relevant or simply phenomena that must be taken into account when studying the high-affinity effects. Additional studies will also be necessary to determine the kinetics, magnitude and direction of Zn^{2+} effects on native $Ca_v2.3$ channels in different cells under physiological conditions, as they could be influenced by a number of factors such as RMP, subunit-composition or alternative splicing. For example, $Ca_vβ$-subunits have been shown to differentially modify the time course of $Ca_v2.3$ channel recovery from inactivation at depolarized test potentials (Jeziorski et al., 2000) as well as the gating effects of Ni^{2+} on cloned $Ca_v2.1$ channels (Zamponi et al., 1996), suggesting that auxiliary subunits could directly or indirectly influence trace metal-induced VGCC modulation.

Limitations

There are some important limitations and inherent assumptions of our work that need to be addressed. First of all, to reduce uncertainty with regard to the K_{Zn} and E_{max} values we analyzed all of the concentration–response relationships using a Hill slope of unity, which assumes simple, bimolecular reactions. With regard to the high-affinity shift and slowing, this assumption seems justified based on the proposed structure of the trace metal binding site. Moreover, when the data were fitted with unconstrained Hill slopes, the values obtained for the high-affinity component were always close to 1 (i.e., 0.7–1.2). Likewise, the Hill slope obtained for the low-affinity slowing after DEPC pretreatment was 0.9 (CI, 0.7–1.0). The low-affinity shift could often be equally well described using different values for the Hill slope, possibly because full saturation of this effect was not consistently observed and/or nonspecific surface charge effects contributed to the net Zn^{2+} action (but see below). However, by fixing the Hill slope to 1, we still obtained visibly good fits, adjusted χ^2 values close to 1, and consistent results for the E_{max} values, suggesting that the plateau phase was sufficiently well defined by the data.

Second, we used DEPC to probe the role of histidine residues for high-affinity Zn^{2+} binding, which is frequently employed for this purpose (Choi and Lipton, 1999; Bancila et al., 2005; Harvey et al., 1999) but has no perfect target specificity and can also react with other amino acid residues (Mendoza and Vachet, 2008; Limpikirati et al., 2019). Protons often compete with Zn^{2+} for binding to the histidine imidazole ring, so that their

effects on Zn^{2+}-induced modulation can to some extent support or oppose an action at histidine residues. For example, moderate acidification reduced the K_{Zn} and E_{max} values for high-affinity shift and slowing and produced effects similar to Zn^{2+} under control conditions, which is consistent with an effect mediated by the known loop histidines. Also, neither DEPC nor acidification altered the concentration dependence of low-affinity slowing, suggesting that histidine residues are not involved and that Zn^{2+} binding to the underlying site was unaffected. On the other hand, DEPC pretreatment completely prevented and partly reversed the Zn^{2+}-induced changes in activation slope factor, while moderate acidification only slightly reduced apparent Zn^{2+} affinity and even increased the maximum Zn^{2+} effects. Likewise, DEPC and protons both reduced the voltage dependence of block/low-affinity II-V current suppression, but DEPC did so by increasing apparent Zn^{2+} affinity at negative test potentials, while protons reduced apparent Zn^{2+} affinity at positive test potential. As such, further studies will clearly be required for firm conclusions with regard to the exact identity of residues that could be directly or indirectly involved in some of the more complex Zn^{2+}-induced effects and their modification by DEPC and protons.

We have also neglected any contribution of nonspecific surface charge screening or binding to the observed effects, which might have introduced some error, especially at the highest free Zn^{2+} levels examined. However, divalent cation concentrations in our recording solutions were relatively high even before addition of Zn^{2+}, and there was no significant difference in channel voltage dependence between recordings performed with 2 versus 4 mM Ca^{2+} or 4 mM Ca^{2+} versus Mg^{2+}, suggesting that the contribution of nonspecific surface charge effects was small.

Finally, although our Markov model for $Ca_v2.3$ channel gating and Zn^{2+}-induced modulation describes well many qualitative and quantitative features of the experimental data, it should be considered preliminary for several reasons. First of all, our model obviously represents a considerable simplification, and the available data are insufficient for a detailed physical interpretation or full validation of the underlying assumptions. The most important limitation in its current form is that the VSMs in the model cannot be related to specific domains in the channel protein, even though its success in modeling the high-affinity Zn^{2+} effects makes it tempting to propose that VSM 1 in the model could correspond to the VSM in domain I. Another related shortcoming of our model is that the state dependence of inactivation had to be determined from the data using an empirical approach. While somewhat arbitrary, this approach was sufficient to demonstrate that Zn^{2+}-induced changes in activation gating alone could bring about the observed changes in inactivation kinetics and voltage dependence if inactivation is state dependent and coupled to activation. Moreover, once exact fluorescence data on $Ca_v2.3$ channel voltage-sensor movement and activation inactivation coupling become available, it should be possible to revise and extent the model structure accordingly.

Lastly, our model in its current form does not reproduce the kinetics of recovery from inactivation or the process of ultraslow inactivation, which we have shown here to be of potential importance for the time course and direction of slow Zn^{2+} effects at depolarized RMPs. Despite all these limitations, we think it is useful to present our model at this time, since it may provide a basis for further investigation of trace metal effects on $Ca_v2.3$ channel function and could be extended based on future findings to ultimately help predict the intricate effects of endogenous Zn^{2+} on neuronal excitability.

Conclusion

The present study performed a comprehensive assessment of the modulation of $Ca_v2.3$ channel electrophysiological properties by a wide range of Zn^{2+} concentrations and reveals how the degree and even direction of effects could be influenced by the prevailing neuronal properties and ionic conditions. While still far from complete, the model developed provides a first quantitative framework for understanding Zn^{2+} effects on $Ca_v2.3$ channel function and a step toward the application of computational approaches for predicting the complex actions of Zn^{2+} on neuronal excitability.

Acknowledgments

Christopher J. Lingle served as editor.

We thank Renate Clemens for her excellent technical assistance.

This work was financially supported by the Köln Fortune Program/Faculty of Medicine, University of Cologne (259/2013) and the Deutsche Forschungsgemeinschaft (SCHN 387/21-1 and SCHN 387/21-2).

The authors declare no competing financial interests.

Author contributions: F. Neumaier was involved in conceptualization, formal analysis, funding acquisition, investigation, methodology, visualization, and writing (original draft, review, and editing). T. Schneider was involved in conceptualization, funding acquisition, project administration, supervision, and writing (review and editing). S. Alpdogan and J. Hescheler contributed resources.

Submitted: 7 February 2020
Revised: 30 April 2020
Accepted: 19 May 2020

References

Aniksztejn, L., G. Charton, and Y. Ben-Ari. 1987. Selective release of endogenous zinc from the hippocampal mossy fibers in situ. *Brain Res.* 404: 58–64. https://doi.org/10.1016/0006-8993(87)91355-2

Assaf, S.Y., and S.-H. Chung. 1984. Release of endogenous Zn^{2+} from brain tissue during activity. *Nature.* 308:734–736. https://doi.org/10.1038/308734a0

Austin, P.C., and J.E. Hux. 2002. A brief note on overlapping confidence intervals. *J. Vasc. Surg.* 36:194–195. https://doi.org/10.1067/mva.2002.125015

Bancila, V., T. Cens, D. Monnier, F. Chanson, C. Faure, Y. Dunant, and A. Bloc. 2005. Two SUR1-specific histidine residues mandatory for zinc-induced activation of the rat K_{ATP} channel. *J. Biol. Chem.* 280:8793–8799. https://doi.org/10.1074/jbc.M413426200

Benison, G., J. Keizer, L.M. Chalupa, and D.W. Robinson. 2001. Modeling temporal behavior of postnatal cat retinal ganglion cells. *J. Theor. Biol.* 210:187–199. https://doi.org/10.1006/jtbi.2000.2289

Besser, L., E. Chorin, I. Sekler, W.F. Silverman, S. Atkin, J.T. Russell, and M. Hershfinkel. 2009. Synaptically released zinc triggers metabotropic

signaling via a zinc-sensing receptor in the hippocampus. *J. Neurosci.* 29: 2890–2901. https://doi.org/10.1523/JNEUROSCI.5093-08.2009

Beyl, S., A. Hohaus, S. Andranovits, E. Timin, and S. Hering. 2016. Upward movement of IS4 and IIIS4 is a rate-limiting stage in $Ca_v1.2$ activation. *Pflugers Arch.* 468:1895–1907. https://doi.org/10.1007/s00424-016-1895-5

Boyett, M.R., H. Honjo, S.M. Harrison, W.-J. Zang, and M.S. Kirby. 1994. Ultra-slow voltage-dependent inactivation of the calcium current in guinea-pig and ferret ventricular myocytes. *Pflugers Arch.* 428:39–50. https://doi.org/10.1007/BF00374750

Brent, R.. 1976. A New Algorithm for Minimizing a Function of Several Variables without Calculating Derivatives. *In* Algorithms for Minimization without Derivatives. Prentice Hall, Englewood Cliffs, NJ. pp. 200–248.

Brog-Graham, L.J.. 1991. Modeling the Nonlinear Conductances of Excitable Membranes. *In* Cellular and Molecular Neurobiology: A Practical Approach. H. Wheal, and J. Chad, editors. Oxford University Press, New York. pp. 247–275.

Capes, D.L., M.P. Goldschen-Ohm, M. Arcisio-Miranda, F. Bezanilla, and B. Chanda. 2013. Domain IV voltage-sensor movement is both sufficient and rate limiting for fast inactivation in sodium channels. *J. Gen. Physiol.* 142:101–112. https://doi.org/10.1085/jgp.201310998

Carnevale, N.T., and M.L. Hines. 2006. The NEURON Book. Cambridge University Press, Cambridge, UK. 742 pp. https://doi.org/10.1017/CBO9780511541612

Castelli, L., F. Tanzi, V. Taglietti, and J. Magistretti. 2003. Cu^{2+}, Co^{2+}, and Mn^{2+} modify the gating kinetics of high-voltage-activated Ca^{2+} channels in rat palaeocortical neurons. *J. Membr. Biol.* 195:121–136. https://doi.org/10.1007/s00232-003-0614-2

Cataldi, M., V. Lariccia, V. Marzaioli, A. Cavaccini, G. Curia, D. Viggiano, L.M.T. Canzoniero, G. di Renzo, M. Avoli, and L. Annunziato. 2007. $Zn(^{2+})$ slows down $Ca_{(v)}3.3$ gating kinetics: implications for thalamocortical activity. *J. Neurophysiol.* 98:2274–2284. https://doi.org/10.1152/jn.00889.2006

Catterall, W.A.. 1998. Structure and function of neuronal Ca^{2+} channels and their role in neurotransmitter release. *Cell Calcium.* 24:307–323. https://doi.org/10.1016/S0143-4160(98)90055-0

Cens, T., M. Rousset, and P. Charnet. 2011. Two sets of amino acids of the domain I of $Ca_v2.3$ $Ca^{(2+)}$ channels contribute to their high sensitivity to extracellular protons. *Pflugers Arch.* 462:303–314. https://doi.org/10.1007/s00424-011-0974-x

Chanda, B., and F. Bezanilla. 2002. Tracking voltage-dependent conformational changes in skeletal muscle sodium channel during activation. *J. Gen. Physiol.* 120:629–645. https://doi.org/10.1085/jgp.20028679

Chen, L.Q., V. Santarelli, R. Horn, and R.G. Kallen. 1996. A unique role for the S4 segment of domain 4 in the inactivation of sodium channels. *J. Gen. Physiol.* 108:549–556. https://doi.org/10.1085/jgp.108.6.549

Choi, Y.-B., and S.A. Lipton. 1999. Identification and mechanism of action of two histidine residues underlying high-affinity Zn^{2+} inhibition of the NMDA receptor. *Neuron.* 23:171–180. https://doi.org/10.1016/S0896-6273(00)80763-1

Christie, B.R., L.S. Eliot, K. Ito, H. Miyakawa, and D. Johnston. 1995. Different Ca^{2+} channels in soma and dendrites of hippocampal pyramidal neurons mediate spike-induced Ca^{2+} influx. *J. Neurophysiol.* 73:2553–2557. https://doi.org/10.1152/jn.1995.73.6.2553

Díaz, D., R. Bartolo, D.M. Delgadillo, F. Higueldo, and J.C. Gomora. 2005. Contrasting effects of Cd^{2+} and Co^{2+} on the blocking/unblocking of human Ca_v3 channels. *J. Membr. Biol.* 207:91–105. https://doi.org/10.1007/s00232-005-0804-1

Dibué-Adjei, M., M.A. Kamp, S. Alpdogan, E.E. Tevoufouet, W.F. Neiss, J. Hescheler, and T. Schneider. 2017. $Ca_v2.3$ (R-type) calcium channels are critical for mediating anticonvulsive and neuroprotective properties of lamotrigine in vivo. *Cell. Physiol. Biochem.* 44:935–947. https://doi.org/10.1159/000485361

Dietrich, D., T. Kirschstein, M. Kukley, A. Pereverzev, C. von der Brelie, T. Schneider, and H. Beck. 2003. Functional specialization of presynaptic $Ca_v2.3$ Ca^{2+} channels. *Neuron.* 39:483–496. https://doi.org/10.1016/S0896-6273(03)00430-6

Drobinskaya, I., F. Neumaier, A. Pereverzev, J. Hescheler, and T. Schneider. 2015. Diethyldithiocarbamate-mediated zinc ion chelation reveals role of $Ca_v2.3$ channels in glucagon secretion. *Biochim. Biophys. Acta.* 1853: 953–964. https://doi.org/10.1016/j.bbamcr.2015.01.001

Du, J., V. Vegh, and D.C. Reutens. 2019. Small changes in synaptic gain lead to seizure-like activity in neuronal network at criticality. *Sci. Rep.* 9:1097. https://doi.org/10.1038/s41598-018-37646-9

Elinder, F., and P. Arhem. 2003. Metal ion effects on ion channel gating. *Q. Rev. Biophys.* 36:373–427. https://doi.org/10.1017/S0033583504003932

Erreger, K., and S.F. Traynelis. 2005. Allosteric interaction between zinc and glutamate binding domains on NR2A causes desensitization of NMDA receptors. *J. Physiol.* 569:381–393. https://doi.org/10.1113/jphysiol.2005.095497

Fass, D.M., and E.S. Levitan. 1996. L-type Ca^{2+} channels access multiple open states to produce two components of Bay K 8644-dependent current in GH3 cells. *J. Gen. Physiol.* 108:13–26. https://doi.org/10.1085/jgp.108.1.13

Flucher, B.E.. 2016. Specific contributions of the four voltage-sensing domains in L-type calcium channels to gating and modulation. *J. Gen. Physiol.* 148:91–95. https://doi.org/10.1085/jgp.201611663

Frederickson, C.J., S.W. Suh, D. Silva, C.J. Frederickson, and R.B. Thompson. 2000. Importance of zinc in the central nervous system: the zinc-containing neuron. *J. Nutr.* 130(5S, Suppl):1471S–1483S. https://doi.org/10.1093/jn/130.5.1471S

Frederickson, C.J., J.-Y. Koh, and A.I. Bush. 2005. The neurobiology of zinc in health and disease. *Nat. Rev. Neurosci.* 6:449–462. https://doi.org/10.1038/nrn1671

García, J., J. Nakai, K. Imoto, and K.G. Beam. 1997. Role of S4 segments and the leucine heptad motif in the activation of an L-type calcium channel. *Biophys. J.* 72:2515–2523. https://doi.org/10.1016/S0006-3495(97)78896-9

Gasparini, S., A.M. Kasyanov, D. Pietrobon, L.L. Voronin, and E. Cherubini. 2001. Presynaptic R-type calcium channels contribute to fast excitatory synaptic transmission in the rat hippocampus. *J. Neurosci.* 21:8715–8721. https://doi.org/10.1523/JNEUROSCI.21-22-08715.2001

Goldberg, R.N., N. Kishore, and R.M. Lennen. 2002. Thermodynamic quantities for the ionization reaction of buffers. *J. Phys. Chem. Ref. Data.* 31: 231–370. https://doi.org/10.1063/1.1416902

Goldschen-Ohm, M.P., D.L. Capes, K.M. Oelstrom, and B. Chanda. 2013. Multiple pore conformations driven by asynchronous movements of voltage sensors in a eukaryotic sodium channel. *Nat. Commun.* 4:1350. https://doi.org/10.1038/ncomms2356

Hamill, O.P., A. Marty, E. Neher, B. Sakmann, and F.J. Sigworth. 1981. Improved patch-clamp techniques for high-resolution current recording from cells and cell-free membrane patches. *Pflugers Arch.* 391:85–100. https://doi.org/10.1007/BF00656997

Harvey, R.J., P. Thomas, C.H. James, A. Wilderspin, and T.G. Smart. 1999. Identification of an inhibitory Zn^{2+} binding site on the human glycine receptor α_1 subunit. *J. Physiol.* 520:53–64. https://doi.org/10.1111/j.1469-7793.1999.00053.x

Hofmann, F., L. Lacinová, and N. Klugbauer. 1999. Voltage-Dependent Calcium Channels: From Structure to Function. *In* Reviews of Physiology, Biochemistry and Pharmacology. Vol. Vol. 139. Springer-Verlag, Berlin, Heidelberg. pp. 33–87.

Howell, G.A., M.G. Welch, and C.J. Frederickson. 1984. Stimulation-induced uptake and release of zinc in hippocampal slices. *Nature.* 308:736–738. https://doi.org/10.1038/308736a0

Jeziorski, M.C., R.M. Greenberg, and P.A.V. Anderson. 2000. Calcium channel β subunits differentially modulate recovery of the channel from inactivation. *FEBS Lett.* 483:125–130. https://doi.org/10.1016/S0014-5793(00)02098-6

Jing, X., D.-Q. Li, C.S. Olofsson, A. Salehi, V.V. Surve, J. Caballero, R. Ivarsson, I. Lundquist, A. Pereverzev, T. Schneider, et al. 2005. $Ca_V2.3$ calcium channels control second-phase insulin release. *J. Clin. Invest.* 115: 146–154. https://doi.org/10.1172/JCI200522518

Josephson, I.R.. 1997. Kinetic components of the gating currents of human cardiac L-type Ca^{2+} channels. *Pflugers Arch.* 433:321–329. https://doi.org/10.1007/s004240050283

Josephson, I.R., and G. Varadi. 1996. The beta subunit increases Ca^{2+} currents and gating charge movements of human cardiac L-type Ca^{2+} channels. *Biophys. J.* 70:1285–1293. https://doi.org/10.1016/S0006-3495(96)79685-6

Kang, H.-W., H.J. Moon, S.H. Joo, and J.-H. Lee. 2007. Histidine residues in the IS3-IS4 loop are critical for nickel-sensitive inhibition of the $Ca_v2.3$ calcium channel. *FEBS Lett.* 581:5774–5780. https://doi.org/10.1016/j.febslet.2007.11.045

Kay, A.R., and R.K. Wong. 1987. Calcium current activation kinetics in isolated pyramidal neurones of the Ca1 region of the mature guinea-pig hippocampus. *J. Physiol.* 392:603–616. https://doi.org/10.1113/jphysiol.1987.sp016799

Khalil, M.M., A.M. Radalla, and A.G. Mohamed. 2009. Potentiometric investigation on complexation of divalent transition metal ions with some zwitterionic buffers and triazoles. *J. Chem. Eng. Data.* 54:3261–3272. https://doi.org/10.1021/je9002459

Kim, B.J., Y.H. Kim, S. Kim, J.W. Kim, J.-Y. Koh, S.H. Oh, M.K. Lee, K.W. Kim, and M.S. Lee. 2000. Zinc as a paracrine effector in pancreatic islet cell death. *Diabetes.* 49:367–372. https://doi.org/10.2337/diabetes.49.3.367

Kodirov, S.A., S. Takizawa, J. Joseph, E.R. Kandel, G.P. Shumyatsky, and V.Y. Bolshakov. 2006. Synaptically released zinc gates long-term potentiation in fear conditioning pathways. *Proc. Natl. Acad. Sci. USA*. 103: 15218–15223. https://doi.org/10.1073/pnas.0607131103

Komatsu, K., K. Kikuchi, H. Kojima, Y. Urano, and T. Nagano. 2005. Selective zinc sensor molecules with various affinities for Zn^{2+}, revealing dynamics and regional distribution of synaptically released Zn^{2+} in hippocampal slices. *J. Am. Chem. Soc.* 127:10197–10204. https://doi.org/10.1021/ja050301e

Kostyuk, P.G., O.A. Krishtal, and Y.A. Shakhovalov. 1977. Separation of sodium and calcium currents in the somatic membrane of mollusc neurones. *J. Physiol*. 270:545–568. https://doi.org/10.1113/jphysiol.1977.sp011968

Li, Y., C.J. Hough, S.W. Suh, J.M. Sarvey, and C.J. Frederickson. 2001. Rapid translocation of $Zn^{(2+)}$ from presynaptic terminals into postsynaptic hippocampal neurons after physiological stimulation. *J. Neurophysiol.* 86:2597–2604. https://doi.org/10.1152/jn.2001.86.5.2597

Limpikirati, P., X. Pan, and R.W. Vachet. 2019. Covalent labeling with Diethylpyrocarbonate: Sensitive to the residue microenvironment, providing improved analysis of protein higher order structure by mass spectrometry. *Anal. Chem*. 91:8516–8523. https://doi.org/10.1021/acs.analchem.9b01732

Lopin, K.V., I.P. Gray, C.A. Obejero-Paz, F. Thévenod, and S.W. Jones. 2012. Fe^{2+} block and permeation of CaV3.1 (α1G) T-type calcium channels: candidate mechanism for non-transferrin-mediated Fe^{2+} influx. *Mol. Pharmacol.* 82:1194–1204. https://doi.org/10.1124/mol.112.080184

Magee, J.C., and M. Carruth. 1999. Dendritic voltage-gated ion channels regulate the action potential firing mode of hippocampal CA1 pyramidal neurons. *J. Neurophysiol.* 82:1895–1901. https://doi.org/10.1152/jn.1999.82.4.1895

Magistretti, J., S. Brevi, and M. de Curtis. 2001. Ni^{2+} slows the activation kinetics of high-voltage-activated Ca^{2+} currents in cortical neurons: evidence for a mechanism of action independent of channel-pore block. *J. Membr. Biol.* 179:243–262. https://doi.org/10.1007/s002320010050

Magistretti, J., L. Castelli, V. Taglietti, and F. Tanzi. 2003. Dual effect of Zn^{2+} on multiple types of voltage-dependent Ca^{2+} currents in rat palaeocortical neurons. *Neuroscience*. 117:249–264. https://doi.org/10.1016/S0306-4522(02)00865-5

Mathie, A., G.L. Sutton, C.E. Clarke, and E.L. Veale. 2006. Zinc and copper: pharmacological probes and endogenous modulators of neuronal excitability. *Pharmacol. Ther*. 111:567–583. https://doi.org/10.1016/j.pharmthera.2005.11.004

Matsuda, Y., H. Saegusa, S. Zong, T. Noda, and T. Tanabe. 2001. Mice lacking $Ca_{(v)}2.3$ (alpha1E) calcium channel exhibit hyperglycemia. *Biochem. Biophys. Res. Commun.* 289:791–795. https://doi.org/10.1006/bbrc.2001.6051

McDougal, R.A., T.M. Morse, T. Carnevale, L. Marenco, R. Wang, M. Migliore, P.L. Miller, G.M. Shepherd, and M.L. Hines. 2017. Twenty years of ModelDB and beyond: building essential modeling tools for the future of neuroscience. *J. Comput. Neurosci*. 42:1–10. https://doi.org/10.1007/s10827-016-0623-7

Mehrke, G., A. Pereverzev, H. Grabsch, J. Hescheler, and T. Schneider. 1997. Receptor-mediated modulation of recombinant neuronal class E calcium channels. *FEBS Lett*. 408:261–270. https://doi.org/10.1016/S0014-5793(97)00437-7

Mendoza, V.L., and R.W. Vachet. 2008. Protein surface mapping using diethylpyrocarbonate with mass spectrometric detection. *Anal. Chem*. 80: 2895–2904. https://doi.org/10.1021/ac701999b

Mohamed, M.M.A.. 2007. Complex formation reactions of lanthanum(III), cerium(III), thorium(IV), dioxouranyl(IV) complexes with tricine. *Ann. Chim*. 97:759–770. https://doi.org/10.1002/adic.200790059

Nakashima, Y.M., S.M. Todorovic, A. Pereverzev, J. Hescheler, T. Schneider, and C.J. Lingle. 1998. Properties of Ba2+ currents arising from human α1E and α1Ebeta3 constructs expressed in HEK293 cells: physiology, pharmacology, and comparison to native T-type Ba2+ currents. *Neuropharmacology*. 37:957–972. https://doi.org/10.1016/S0028-3908(98)00097-5

Nakayama, S., and A.F. Brading. 1993. Evidence for multiple open states of the Ca^{2+} channels in smooth muscle cells isolated from the guinea-pig detrusor. *J. Physiol*. 471:87–105. https://doi.org/10.1113/jphysiol.1993.sp019892

Neumaier, F., M. Dibué-Adjei, J. Hescheler, and T. Schneider. 2015. Voltage-gated calcium channels: Determinants of channel function and modulation by inorganic cations. *Prog. Neurobiol*. 129:1–36. https://doi.org/10.1016/j.pneurobio.2014.12.003

Neumaier, F., S. Alpdogan, J. Hescheler, and T. Schneider. 2017. A practical guide to the preparation and use of metal ion-buffered systems for physiological research. *Acta Physiol. (Oxf.)*. 12988. https://doi.org/10.1111/apha.12988

Noh, J., M.K. Kim, and J.M. Chung. 2010. A novel mechanism of zinc block on alpha1G-like low-threshold T-type Ca^{2+} channels in a rat thalamic relay neuron. *Neurosci. Res*. 66:353–358. https://doi.org/10.1016/j.neures.2009.12.005

Pan, E., X.-A. Zhang, Z. Huang, A. Krezel, M. Zhao, C.E. Tinberg, S.J. Lippard, and J.O. McNamara. 2011. Vesicular zinc promotes presynaptic and inhibits postsynaptic long-term potentiation of mossy fiber-CA3 synapse. *Neuron*. 71:1116–1126. https://doi.org/10.1016/j.neuron.2011.07.019

Pantazis, A., N. Savalli, D. Sigg, A. Neely, and R. Olcese. 2014. Functional heterogeneity of the four voltage sensors of a human L-type calcium channel. *Proc. Natl. Acad. Sci. USA*. 111:18381–18386. https://doi.org/10.1073/pnas.1411127112

Park, S.-J., S.-H. Min, H.-W. Kang, and J.-H. Lee. 2015. Differential zinc permeation and blockade of L-type Ca^{2+} channel isoforms $Ca_v1.2$ and $Ca_v1.3$. *Biochim. Biophys. Acta*. 1848(10, 10 Pt A):2092–2100. https://doi.org/10.1016/j.bbamem.2015.05.021

Pereverzev, A., M. Mikhna, R. Vajna, C. Gissel, M. Henry, M. Weiergräber, J. Hescheler, N. Smyth, and T. Schneider. 2002. Disturbances in glucose-tolerance, insulin-release, and stress-induced hyperglycemia upon disruption of the $Ca_{(v)}2.3$ (α_{1E}) subunit of voltage-gated $Ca^{(2+)}$ channels. *Mol. Endocrinol.* 16:884–895. https://doi.org/10.1210/mend.16.4.0801

Pereverzev, A., A. Salehi, M. Mikhna, E. Renström, J. Hescheler, M. Weiergräber, N. Smyth, and T. Schneider. 2005. The ablation of the $Ca_{(v)}2.3$/E-type voltage-gated Ca^{2+} channel causes a mild phenotype despite an altered glucose induced glucagon response in isolated islets of Langerhans. *Eur. J. Pharmacol*. 511:65–72. https://doi.org/10.1016/j.ejphar.2005.01.044

Qian, J., and J.L. Noebels. 2005. Visualization of transmitter release with zinc fluorescence detection at the mouse hippocampal mossy fibre synapse. *J. Physiol*. 566:747–758. https://doi.org/10.1113/jphysiol.2005.089276

Qian, J., and J.L. Noebels. 2006. Exocytosis of vesicular zinc reveals persistent depression of neurotransmitter release during metabotropic glutamate receptor long-term depression at the hippocampal CA3-CA1 synapse. *J. Neurosci*. 26:6089–6095. https://doi.org/10.1523/JNEUROSCI.0475-06.2006

Quinta-Ferreira, M.E., F.D.S. Sampaio Dos Aidos, C.M. Matias, P.J. Mendes, J.C. Dionísio, R.M. Santos, L.M. Rosário, and R.M. Quinta-Ferreira. 2016. Modelling zinc changes at the hippocampal mossy fiber synaptic cleft. *J. Comput. Neurosci*. 41:323–337. https://doi.org/10.1007/s10827-016-0620-x

Sala, F.. 1991. Activation kinetics of calcium currents in bull-frog sympathetic neurones. *J. Physiol*. 437:221–238. https://doi.org/10.1113/jphysiol.1991.sp018592

Savalli, N., A. Pantazis, D. Sigg, J.N. Weiss, A. Neely, and R. Olcese. 2016. The $\alpha_2\delta$-$_1$ subunit remodels $Ca_V1.2$ voltage sensors and allows Ca^{2+} influx at physiological membrane potentials. *J. Gen. Physiol*. 148:147–159. https://doi.org/10.1085/jgp.201611586

Schneider, T., X. Wei, R. Olcese, J.L. Costantin, A. Neely, P. Palade, E. Perez-Reyes, N. Qin, J. Zhou, G.D. Crawford, et al. 1994. Molecular analysis and functional expression of the human type E neuronal Ca^{2+} channel alpha 1 subunit. *Receptors Channels*. 2:255–270.

Shcheglovitov, A., I. Vitko, R.M. Lazarenko, P. Orestes, S.M. Todorovic, and E. Perez-Reyes. 2012. Molecular and biophysical basis of glutamate and trace metal modulation of voltage-gated $Ca_{(v)}2.3$ calcium channels. *J. Gen. Physiol*. 139:219–234. https://doi.org/10.1085/jgp.201110699

Sivagnanam, S., A. Majumdar, K. Yoshimoto, V. Astakhov, and A. Bandrowski. M.M. E., and N.T. Carnevale. 2013. Introducing the Neuroscience Gateway. *In* CEUR Workshop Proceedings. Vol. 993.

Sochivko, D., A. Pereverzev, N. Smyth, C. Gissel, T. Schneider, and H. Beck. 2002. The $Ca_{(V)}2.3$ $Ca^{(2+)}$ channel subunit contributes to R-type $Ca^{(2+)}$ currents in murine hippocampal and neocortical neurones. *J. Physiol*. 542:699–710. https://doi.org/10.1113/jphysiol.2002.020677

Sun, H.-S., K. Hui, D.W.K. Lee, and Z.-P. Feng. 2007. Zn^{2+} sensitivity of high- and low-voltage activated calcium channels. *Biophys. J*. 93:1175–1183. https://doi.org/10.1529/biophysj.106.103333

Thomas, E.A., C.A. Reid, S.F. Berkovic, and S. Petrou. 2009. Prediction by modeling that epilepsy may be caused by very small functional changes in ion channels. *Arch. Neurol*. 66:1225–1232. https://doi.org/10.1001/archneurol.2009.219

Traboulsie, A., J. Chemin, M. Chevalier, J.-F. Quignard, J. Nargeot, and P. Lory. 2007. Subunit-specific modulation of T-type calcium channels by zinc. *J. Physiol*. 578:159–171. https://doi.org/10.1113/jphysiol.2006.114496

Ueno, S., M. Tsukamoto, T. Hirano, K. Kikuchi, M.K. Yamada, N. Nishiyama, T. Nagano, N. Matsuki, and Y. Ikegaya. 2002. Mossy fiber Zn^{2+} spillover

modulates heterosynaptic N-methyl-D-aspartate receptor activity in hippocampal CA3 circuits. *J. Cell Biol.* 158:215–220. https://doi.org/10.1083/jcb.200204066

Vergnano, A.M., N. Rebola, L.P. Savtchenko, P.S. Pinheiro, M. Casado, B.L. Kieffer, D.A. Rusakov, C. Mulle, and P. Paoletti. 2014. Zinc dynamics and action at excitatory synapses. *Neuron.* 82:1101–1114. https://doi.org/10.1016/j.neuron.2014.04.034

Vogt, K., J. Mellor, G. Tong, and R. Nicoll. 2000. The actions of synaptically released zinc at hippocampal mossy fiber synapses. *Neuron.* 26:187–196. https://doi.org/10.1016/S0896-6273(00)81149-6

Weiergräber, M., M. Henry, A. Krieger, M. Kamp, K. Radhakrishnan, J. Hescheler, and T. Schneider. 2006a. Altered seizure susceptibility in mice lacking the $Ca_{(v)}2.3$ E-type Ca^{2+} channel. *Epilepsia.* 47:839–850. https://doi.org/10.1111/j.1528-1167.2006.00541.x

Weiergräber, M., M.A. Kamp, K. Radhakrishnan, J. Hescheler, and T. Schneider. 2006b. The $Ca_{(v)}2.3$ voltage-gated calcium channel in epileptogenesis--shedding new light on an enigmatic channel. *Neurosci. Biobehav. Rev.* 30:1122–1144. https://doi.org/10.1016/j.neubiorev.2006.07.004

Weiergräber, M., M. Henry, K. Radhakrishnan, J. Hescheler, and T. Schneider. 2007. Hippocampal seizure resistance and reduced neuronal excitotoxicity in mice lacking the $Ca_v2.3$ E/R-type voltage-gated calcium channel. *J. Neurophysiol.* 97:3660–3669. https://doi.org/10.1152/jn.01193.2006

Winegar, B.D., R. Kelly, and J.B. Lansman. 1991. Block of current through single calcium channels by Fe, Co, and Ni. Location of the transition metal binding site in the pore. *J. Gen. Physiol.* 97:351–367. https://doi.org/10.1085/jgp.97.2.351

Woodhull, A M. 1973. Ionic blockage of sodium channels in nerve. *J. Gen. Physiol.* 61(6):687–708. https://doi.org/10.1085/jgp.61.6.687

Yasuda, T., R.J. Lewis, and D.J. Adams. 2004. Overexpressed $Ca_{(v)}\beta_3$ inhibits N-type ($Ca_v2.2$) calcium channel currents through a hyperpolarizing shift of ultra-slow and closed-state inactivation. *J. Gen. Physiol.* 123:401–416. https://doi.org/10.1085/jgp.200308967

Zamponi, G.W., E. Bourinet, and T.P. Snutch. 1996. Nickel block of a family of neuronal calcium channels: subtype- and subunit-dependent action at multiple sites. *J. Membr. Biol.* 151:77–90. https://doi.org/10.1007/s002329900059

Zhang, Q., M. Bengtsson, C. Partridge, A. Salehi, M. Braun, R. Cox, L. Eliasson, P.R.V. Johnson, E. Renström, T. Schneider, et al. 2007. R-type $Ca^{(2+)}$-channel-evoked CICR regulates glucose-induced somatostatin secretion. *Nat. Cell Biol.* 9:453–460. https://doi.org/10.1038/ncb1563

Supplemental material

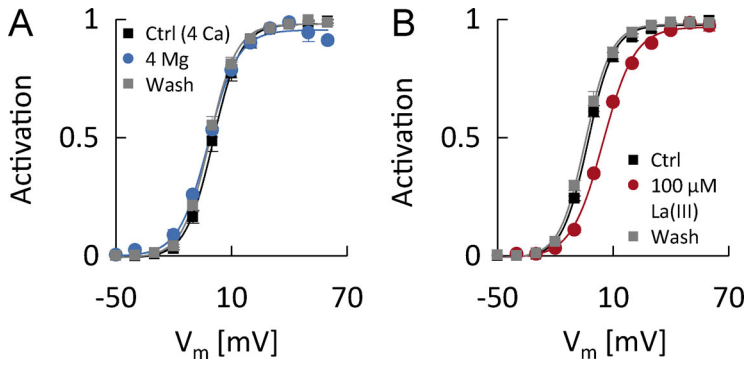

Figure S1. **Effects of Ca^{2+} substitution by Mg^{2+} or ionic block by La^{3+} on $Ca_v2.3$ channel voltage dependence. (A)** Isochronous activation curves constructed from $Ca_v2.3$ channel currents before (black squares), during (blue circles), and after (gray squares) substitution of 4 mM free Ca^{2+} as the charge carrier by 4 mM free Mg^{2+} (n = 5 cells). **(B)** Isochronous activation curves constructed from $Ca_v2.3$ channel currents carried by 4 mM free Ca^{2+} before (black squares), during (red circles), and after (gray squares) application of 100 µM free La^{3+} (n = 6 cells).

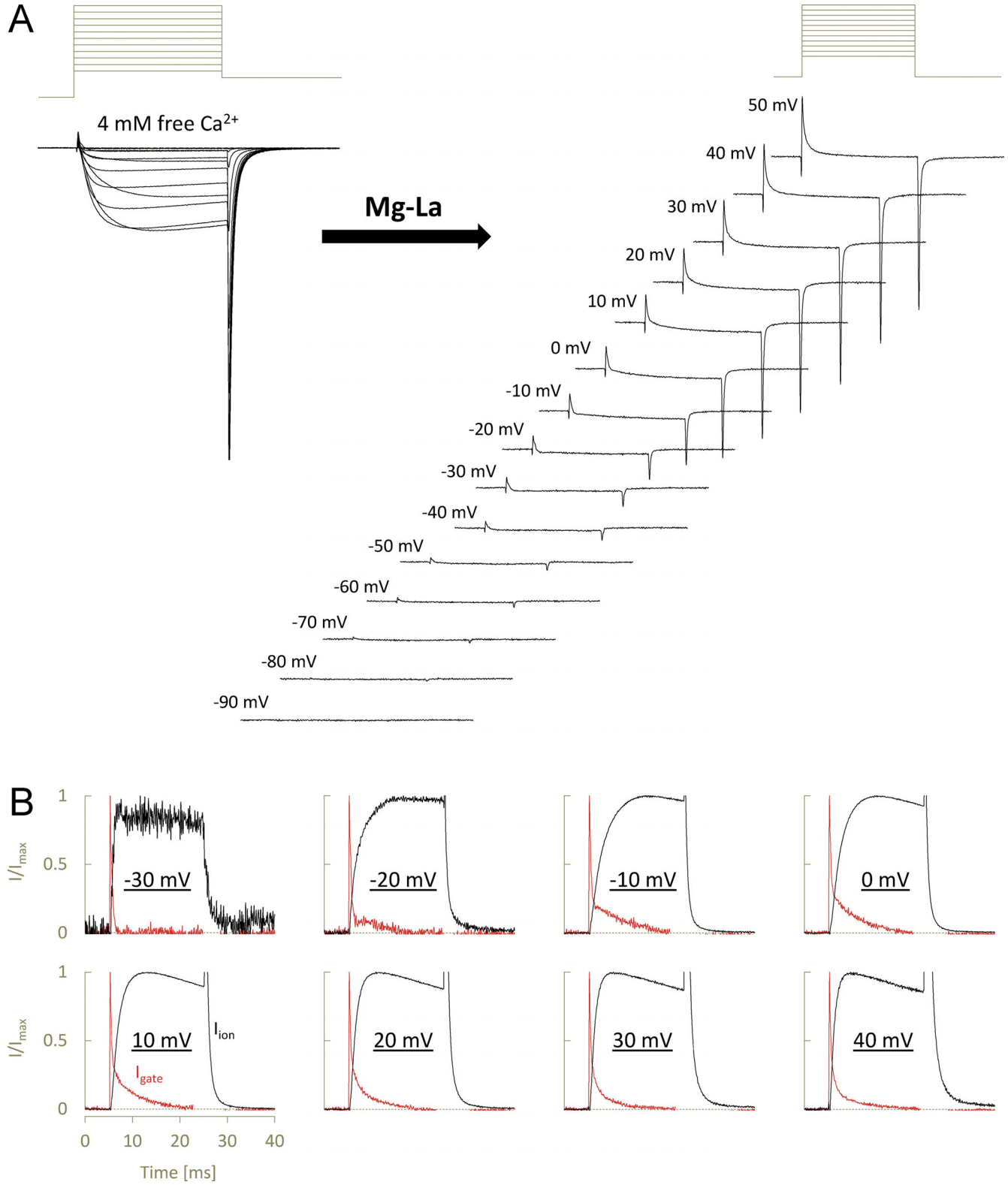

Figure S2. **$Ca_v2.3$ channel ionic and gating currents. (A)** Mean ionic (left) and gating (right) current traces recorded from the same cells before and after Ca^{2+} substitution by Mg^{2+} and addition of 100 µM free La^{3+} (n = 18). Test potentials indicated next to the gating current traces have been corrected for the shift in channel voltage dependence produced by the La^{3+} used to suppress ionic currents. **(B)** Comparison of mean ionic (black) and gating (red) current traces after normalization by their maximum amplitudes to show that there was a significant fraction of charge movement that is too slow to be associated with channel opening (same cells as in A).

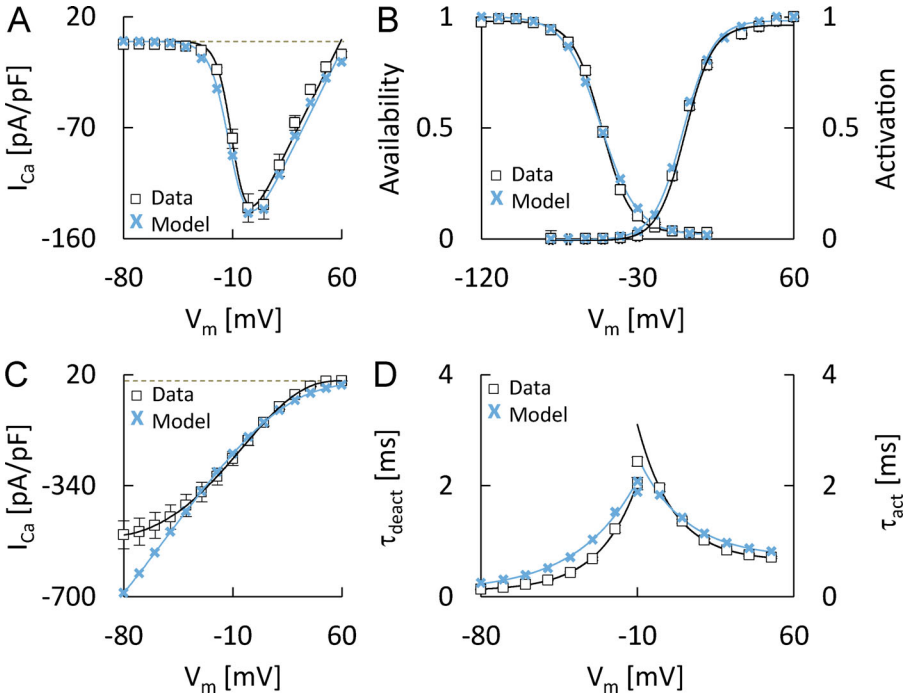

Figure S3. **Modeling $Ca_v2.3$ channel gating under control conditions.** Comparison of I-V relationships (A), activation and PPI curves (B), II-V relationships (C), and activation and deactivation time constants (D), determined in the same way from either experimental control recordings with 4 mM Ca^{2+} as the charge carrier (open squares) or from currents simulated with the model shown in Fig. 15 (turquoise crosses).

Tables S1, S2, S3, S4, and S5 are provided online as separate files. Table S1 lists the composition of different external solutions used in electrophysiological recordings. Table S2 shows the absolute effects of 5.4 µM free Zn^{2+} on $Ca_v2.3$ channel gating under different experimental conditions. Table S3 lists the effects of different free Zn^{2+} concentrations on $Ca_v2.3$ channel gating. Table S4 provides the E_{max} and K_{Zn} values obtained from Zn^{2+} concentration-response data under different experimental conditions. Table S5 provides the global K_{Zn} values for high-affinity shift and slowing.